Vibrated granular matter: transport, fluidization, and patterns

Von der Universität Bayreuth
zur Erlangung des Grades eines
Doktors der Naturwissenschaften (Dr. rer. nat.)
genehmigte Abhandlung

vorgelegt von

Andreas Götzendorfer

geboren am 9. September 1976 in München

Erster Gutachter:	PD Dr. Christof A. Krülle, Universität Bayreuth
Zweiter Gutachter:	Prof. Dr. Ingo Rehberg, Universität Bayreuth
auswärtiger Gutachter:	PD Dr. Thorsten Pöschel, Humboldt-Universität Berlin

Tag der Einreichung:	6. Oktober 2006
Tag des Kolloquiums:	12. Februar 2007

Zusammenfassung

Unter granularer Materie versteht man eine Ansammlung von Teilchen, deren Größe einen Mikrometer überschreitet. Brownsche Bewegung ist dann vernachlässigbar. Ihr Verhalten wurde spätestens seit Charles-Augustin de Coulomb (1736-1806) studiert, der mit seinem Reibungsgesetz den Schüttwinkel von Sandhaufen erklärte. Breites Interesse an granularen Systemen von Seiten der Physik kam um 1990 auf, angetrieben durch die wachsende Leistungsfähigkeit von Computersimulationen. Seitdem ist die Anzahl der Veröffentlichungen auf diesem Gebiet explosionsartig angestiegen.

Da Stöße makroskopischer Körner im Allgemeinen inelastisch sind, muss einem granularen System, um es in Bewegung zu halten, laufend Energie zugeführt werden. In Laborexperimenten wird dies oft durch einen horizontal oder vertikal sinusförmig schwingenden Behälter erreicht. In dieser Arbeit wurde die Auswirkung einer Anregungsform untersucht, bei der horizontale und vertikale Schwingung gleiche Amplitude besitzen und mit einer Phasenverschiebung von $\pi/2$ überlagert sind. Das heißt, jeder Punkt der Unterlage beschreibt eine Kreisbahn. Durch die Wahl einer ringförmigen Behältergeometrie, konnte das Langzeitverhalten eines geschlossenen, Masse erhaltenden Systems studiert werden.

So war es unter anderem möglich, räumlich ausgedehnte Oberflächenmuster in einem granularen Bett zu untersuchen. Innerhalb eines bestimmten Intervalls von Anregungsbeschleunigungen bilden sich auf der Granulatoberfläche stehende Wellen aus, die mit der halben Anregungsfrequenz oszillieren. Die dominierende Wellenlänge wurde für verschiedene Antriebsfrequenzen bei konstant gehaltener Anregungsamplitude gemessen. Die beobachteten Stehwellen sind nicht stationär, sondern driften mit der Transportgeschwindigkeit des granularen Materials, welche mit Hilfe eines Tracerpartikels bestimmt wird.

Bei höherer Anregungsstärke wurden lokalisierte periodenverdoppelnde Stehwellen beobachtet. Diese im Ring umlaufenden, solitären Wellenpakete treten in Verbindung mit einer lokal erhöhten Teilchendichte auf. Die Länge und die Geschwindigkeit des granularen Wellenpulses wurden gemessen und ihre Abhängigkeit von der im Behälter vorhandenen Menge Granulat bestimmt. Inspiriert durch ein bekanntes Modell aus der Straßenverkehrsforschung, welches das plötzliche Auftreten von Pulsen erhöhter Dichte, so genannten “Phantomstaus”, aus anfänglich gleichmäßigem Verkehrsfluß erklärt, wurde

ein einfaches Kontinuumsmodell für die Materialverteilung im Behälterring entwickelt. Basierend auf der gemessenen Transportgeschwindigkeit des Granulats als Funktion der Betthöhe, beschreibt es die wesentlichen experimentellen Ergebnisse korrekt.
Des Weiteren wurde die Fluidisierung einer Monolage Glaskugeln bei zirkularer Vibration untersucht. Bei Spitzenbeschleunigungen innerhalb eines bestimmten Intervalls koexistieren ein Bereich, in dem das Granulat kristallin geordnet ist, und ein Bereich, in dem sich das Granulat in einem gasartigen Zustand befindet. Der kristalline Anteil nimmt mit wachsender Anregungsbeschleunigung ab und zeigt Hysterese. Die scharfen Grenzen zwischen den zwei Regionen laufen im Ring um, und zwar mit einer Geschwindigkeit, die größer ist als die mittlere Transportgeschwindigkeit des Granulats. Komplementär zu den experimentellen Untersuchungen wird mit Hilfe einer molekulardynamischen Simulation die lokale granulare Temperatur, welche im Wesentlichen als die Varianz der Geschwindigkeitsverteilung der Partikel definiert ist, und die Partikeldichte extrahiert. Es zeigt sich, dass die Teilchendichte in der kristallinen Phase ein Vielfaches der Teilchendichte in der gasartigen Phase ist, wohingegen die granulare Temperatur um Größenordnungen kleiner ist.
Um den Übergang einer Kugelpackung mit kristalliner Ordnung in den vollkommen fluidisierten Zustand zu untersuchen wurde ein separates Experiment aufgebaut. Die Bewegung der Partikel wurde auf zwei Dimensionen eingeschränkt, damit sie für die Kamera immer sichtbar bleiben. Mit Hilfe einer Hochgeschwindigkeitskamera konnten die Trajektorien aller Partikel rekonstruiert werden. Die anregende Vibration war ausschließlich vertikal. Antriebsfrequenz und Amplitude wurden in einem weiten Bereich variiert.
Ein anfänglich dicht gepacktes zweidimensionales granulares Bett wurde sinusförmigen Schwingungen des Behälters mit nach und nach steigender Amplitude ausgesetzt. Zuerst fangen die Partikel der obersten Lage an sich zu bewegen. Wird ein kritischer Wert der Antriebsstärke überschritten bricht der restliche Kristall plötzlich auf und das Bett fluidisiert vollständig. Dieser Übergang geht einher mit diskontinuierlichen Änderungen der Dichteverteilung und der mittleren quadratischen Verschiebung der einzelnen Partikel. Außerdem steigt die vertikale Koordinate des Massenschwerpunkts beim Übergang sprunghaft an. Es zeigt sich, dass die maximale Behältergeschwindigkeit v_0 den Zustand des vollständig fluidisierten Systems bestimmt. Partikel unterschiedlicher Größe vollziehen den Übergang alle beim selben Wert der Größe v_0^2/gd, wobei d der Partikeldurchmesser und g die Erdbeschleunigung ist. Ein diskontinuierlicher Fluidisierungsübergang wird allerdings nur beobachtet, wenn die Partikel hoch elastisch sind. Inwieweit diese Ergebnisse auf dreidimensionale Systeme übertragbar sind, ist noch unklar.

Contents

1 Introduction **7**

2 Setup for circularly vibrated granular beds **15**
2.1 Determination of the container motion 19
2.2 Imaging 23

3 Extended surface waves **27**
3.1 Introduction 27
3.2 Experiment 28
3.3 Results and Discussion 28
3.3.1 Wavelength 30
3.3.2 Drift velocity 32
3.4 Conclusion 33

4 Localized subharmonic waves **35**
4.1 Introduction 35
4.2 Experiment 37
4.3 Results 37
4.4 Model 41
4.5 Comparison between simulation and experiment 42
4.6 Conclusion 43

5 Sublimation of a vibrated monolayer **45**
5.1 Introduction 45
5.2 Experiment 46
5.3 Simulation 47
5.4 Results 48
5.5 Conclusion 51

6 Setup for vertically agitated 2D packings **53**

7 Granular meltdown **57**
7.1 Introduction 57
7.2 Results and Discussion 60
7.2.1 The fluidization transition 60
7.2.2 The center of mass height 65
7.3 Summary and conclusion 68

8 Conclusion and Outlook **71**

Acknowledgment **87**

Chapter 1

Introduction

Granular matter is defined as large collection of particles the size of which is larger than one micron so that Brownian motion is negligible. Its behavior has been studied at least since the days of Charles-Augustin de Coulomb (1736-1806), who originally stated his law of friction for granular materials (de Coulomb 1785). An early contribution to the exploration of structure formation phenomena in granular matter came from Michael Faraday (1791-1867) with his explanation of the heaping phenomenon (Faraday 1831), observed by Ernst Florens Friedrich Chladni (1756-1827) in powders on vibrating plates (Chladni 1787). Osborne Reynolds (1842-1912) introduced the principle of dilatancy when he realized that granular matter at a density above a certain critical density can only be deformed under volume expansion (Reynolds 1885). Already these grand masters of physics, celebrated for their achievements in electromagnetism, acoustics, and fluid dynamics were intrigued by the peculiar behavior of granular matter.

The best known examples of granular patters are probably encountered in geomorphology. Ripples and dunes, found in sand deserts like The Empty Quarter (Arabic: Rub' al Khali), the largest sand desert in the world, provide beautiful and impressive examples of complex structures formed by granular assemblies. An outstanding pioneer in desert exploration, Ralph Alger Bagnold (1896-1990) determined the basic laws for wind-driven transport of sand that form the basis of dune formation and evolution. His classic treatise "The physics of blown sand and desert dunes" (Bagnold 1941) has remained a basic reference and is still used to explain the shapes of sand dunes on Mars photographed during the latest NASA and ESA missions to the "Red Planet".

In the physics community interest in granular media started to grow considerably around 1990, driven by the fast-growing performances of computer simulations. Four years later Anita Mehta wrote in one of the first review articles of the field "in recent years, sand has become a paradigm of complexity in physics", and "the last few years have seen an explosion in theoretical and experimental activity in the study of its dynamics". In the

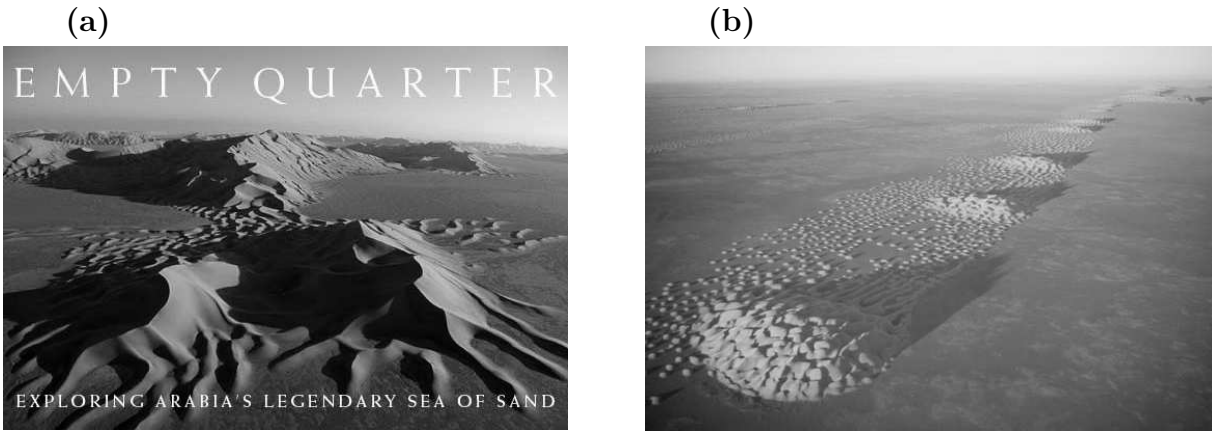

Figure 1.1: Star dunes (a) and complex mega-barcan dunes (b) in the empty quarter. From National Geographic Magazine, Feb. 2005. Photographs by George Steinmetz.

following years granular research has still gained momentum and continues to prosper. Much insight into the behavior of granular matter was gained from experiments and simulations of vertically or horizontally vibrated granular assemblies. Topics of investigations included fluidization, convection, compaction, heaping, clustering, surface waves, segregation etc. The rapid development of research in the field of granular physics has led to a series of review articles covering some of the major activities.

In 1990 Campbell gave an overview of the theory of rapid granular flows, the progress of which had been till then due to the interplay between theoretical models and computer simulations. He ended his concluding remarks by calling on experimentalists to develop procedures capable of making detailed measurements of properties such as velocity, density, and granular temperature profiles in order to resolve persistent controversies.

Bak, Tang, and Wiesenfeld (Bak et al. 1987; Tang and Bak 1988) stirred general interest in granular physics by introducing the notion of self organized criticality to describe the behavior of spatially extended, driven dynamical systems in a steady state. The theory was originally formulated in terms of avalanches in granular systems. Nagel (1992) then caused another sensation when he reviewed experiments on the avalanching dynamics of a sand pile, demonstrating that it does not show self-organized critical behavior.

In 1996 Jaeger et al. presented a bunch of complex phenomena, observed in experiments and computer simulations, where at first glance the granular material resembles a solid, liquid, or gas. Yet on closer inspection the properties of granular materials are always unusual insofar as they are different from those commonly associated with either solids, liquids, or gases. In this sense Mehta and Barker (1994) even speak of a new state of matter, namely the granular state that often exhibits behavior intermediate between that of solids and liquids. Mehta and Barker report on the progress made in extending the knowledge about granular flow in regimes of rapid shear to at least a limited understanding

Figure 1.2: Sand castle erected during the 4th international sand sculpture festival in Travemünde. Photo taken from the www.sandworld.de.

of regimes where grains are in slow, or no motion with respect to one another.
de Gennes (1999) discussed the statics of heaps and silos. He restricted his review to several macroscopic and microscopic approaches to static problems. The main concern of Kadanoff (1999) was with vibrofluidized granular matter. He asked the question whether its dynamics can be described by hydrodynamic equations like those that apply to ordinary fluids. Finally his answer was 'No!', stating that granular systems often show glassy behavior, which is not fully described by a simple set of partial differential equations.
Vibrated mixtures of large and small particles generally tend to segregate. Usually the larger component accumulates at the top, a phenomenon known as Brazil-nut effect, but at certain physical conditions they may also sink to the bottom. An account of advances in the understanding of size separation in shaken granular materials was given by Kudrolli (2004). The size ratio surely is the dominant factor. In addition, particle specific properties like density, inelasticity, and friction as well as the nature of the energy input, the boundary conditions and interstitial air also play important roles.
The above cited articles only treat dry granular media. When liquid is present between the grains the resulting inter-grain cohesion drastically modifies the mechanical properties of the granular media. By moistening sand one can increase the angle of repose above 90°. This allows sand carvers to form structures like the one depicted in Fig. 1.2. Herminghaus (2005) and Mitarai and Nori (2006) give overviews over the behavior of wet granular media. Presented model systems are based on statistical concepts and explain some features of the dynamics and the phase transitions encountered in these systems.
In their recent review on patterns and collective behavior in granular media Aranson and Tsimring (2006) survey the different, often contradictory concepts and approaches devised to describe granular systems. Focusing on patterns, they elucidate the differences

between structure formation phenomena in granular systems and continuum fluids. Some examples are given that show how general principles and models of pattern formation in complex systems were successfully applied to granular systems.
All in all one can say that despite the great efforts committed to learn more about the behavior of granular matter an understanding of its statics and dynamics is still in its infancy and a consistent picture is not yet available.
Mechanical and chemical engineers have long been striving to improve their knowledge about bulk solids since large portions of the material manipulated in industry belong to this category. Because basic understanding lacks, industrial facilities for handling granular materials often operate inefficiently. When designing machines like vibratory conveyors, which are widely used to carry small components, coal pieces, cereal grains, fertilizer granulates, sands, powders, and so on, one is not able to predict their transport properties but has to construct prototypes for empirical testing and tuning.
In order to gain better insight into the behavior of granular matter and to overcome the problems encountered in practice a coordinated approach from physicists and engineers, combining knowledge and techniques from both communities promised to be fruitful. Therefore in march 1999 the German Research Foundation (DFG) established the project-group "Vom Molekül zum Material" (engl.: From molecule to material) creating the administrative and financial basis for the establishment of larger interdisciplinary cooperation between physics/chemistry and mechanical engineering/material science. The initiative "Verhalten Granularer Medien" (engl.: Behavior of granular matter) that emanated from this program bringing together physicists and engineers working in the field of granular matter. It was launched in December 1999 with a main focus on the following four topics:

1. Highly laden suspensions
2. Dry particle flow
3. Electrostatic forces
4. Cohesive granules

Altogether seven mixed teams got together involving researchers from thirteen universities. The coordination lay in the hands of Prof. Walzel from Universität Dortmund und Prof. Herrmann from Universität Stuttgart.
In this thesis, some mayor results obtained in the course of the particular project "Transport Behavior and Structure Formation of Granular Matter on Vibratory Conveyors" are reported. The team working on this project was composed of an experimental and a theoretical group of physicists, directed by PD Krülle (Universität Bayreuth) and Prof. Linz

(Universität Münster) respectively, and a group of process engineers around Prof. Walzel (Universität Dortmund). The common goal was to improve the basic understanding of granular transport and pattern formation on vibrated supports and their interplay.

In the beginning of the project, work was focused on a systematic experimental study of the transport velocity as a function of the type of forcing (Grochowski et al. 2004; Rouijaa et al. 2005; Kruelle et al. 2004; Kruelle et al. 2005). Meanwhile the theory group numerically simulated the motion of the granular bed, modeled as a single block. By skillfully tuning the model parameters they were able to reproduce the experimental results (El hor and Linz 2005; El hor et al. 2005).

In Bayreuth, after this initial phase, the formation of patterns in vibrotransported beds became the center of interest. A vibrated granular assembly represents a perfect example of a driven dissipative system exhibiting nonlinear dynamics. The complex structures that spontaneously appear in these nonequilibrium systems have long intrigued physicists. Previous experiments and simulations of pattern formation in vibrated granular beds mainly employed pure vertical agitation (see Section 3.1). This project addressed the question what kind of patterns arise when an additional horizontal forcing component is present i.e. when the material is transported.

The planned investigations required a machine that superposes sinusoidal horizontal and vertical oscillations allowing an independent variation of the driving parameters like frequency, horizontal and vertical amplitudes as well as the phase relation between horizontal and vertical oscillations. In Dortmund the endeavor to find optimum settings for efficient transport also included trials at various inclination angles of the conveying trough. Experiments on pattern formation were limited to the circular vibration mode, i.e. equal amplitudes of horizontal and vertical oscillation and a phase shift of $\pi/2$. Already with these settings a great wealth of phenomena was discovered, the detailed examination of which absorbed the available time.

The vibration apparatuses were designed and built in Dortmund based on know-how acquired by the group of engineers there during the construction of a forerunner model (Landwehr et al. 1997; Landwehr and Walzel 1999). The machine relies on an unbalanced mass driving already well established in industrial applications like vibratory conveyors, sieving machines and other vibration devices. With the chosen driving system, horizontal and vertical oscillation amplitudes as well as the phase shift between the horizontal and vertical oscillations can be varied by changing the relative orientation and the weight of the mounted unbalanced masses.

The conveying troughs in Dortmund and Bayreuth were shaped as to best meet the respective needs. For the extensive transport velocity measurements carried out in Dortmund a linear geometry proved to be convenient. In the steady state, when the mass flow

$\Phi = \mathrm{d}m/\mathrm{d}t$ fed to the conveyor at one end equals the outflow at the other end, the mean transport velocity v_t was determined by weighing the hold up M, i.e. the total mass in the trough. A simple calculation yields $v_t = \Phi l/M$, where l is the trough length. Patterns in granular matter typically evolve into a steady state on relatively long time scales. Therefore the limited residence time of material in a linear trough ruled out this geometry for the setup in Bayreuth. In contrast an annular container that strictly conserves mass seemed to be the ideal choice for experiments on structure formation. In this way also potential disturbances caused by material feeding and outflow could be avoided.

When the first annular container was designed there were worries about centrifugal forces causing an accumulation of revolving granular material close to the outer channel wall. A rounded channel cross section should counteract this tendency and keep the material in the middle of the trough. When later this channel was replaced by a transparent one with rectangular cross section it turned out that still the surface remained flat in the lateral direction. Obviously in all examined cases diffusion was strong enough to prevent the granulate from accumulating at the outer channel wall.

In their seminal publications on transport of bulk solids on vibratory conveyors Rademacher and Ter Borg (1994), Rademacher (1995), and Sloot and Kruyt (1996) modeled the granular bed as a single plastic body. El hor and Linz adopted this concept for their numerical simulations. Yet to match transport data for beds consisting of highly elastic particles above a certain forcing strength the assumption of complete inelasticity had to be dropped. First approaches to the task of describing vibrotransport of an elastic particle had already been made by Hongler et al. (1989) and Landwehr et al., (1997, 1999), who found a strong dependence on the degree of inelasticity, which is not astonishing taking into account the complex behavior of an elastic object on a vertically oscillating plate exposed by Luck and Mehta (1993).

Plastic behavior of a granular bed is due to energy dissipation by interparticle collisions, which dampen the energy supplied to the lowest particle layer by the container floor. Whether a bed collision is plastic or elastic depends, apart from the forcing strength, very much on the number of particle layers present. In Chapter 5 it will be shown that plastic and elastic behavior can develop in different regions of the container at the same time. An inelastically colliding bed has a reduced density and exists in a sort of gaseous state. Particle collisions with the floor do not happen cooperatively but in an almost random way. In this case modeling the granular bed as a single object is inappropriate. Up to now there is no simple model for the vibrotransport of a granular gas. One resorts to molecular dynamics (MD) simulations that resolve the motion of individual particles. Chapter 5 sets forth the combined approach of experiments and event-driven MD simulations to elucidate the sublimation of a monolayer of glass beads. In simulations one can easily vary

parameters and sort out the necessary conditions for the occurrence of a phenomenon. Furthermore, the availability of particle positions and velocities at all times opens the way for a more advanced and deeper analysis of the system. For example the granular temperature, defined as the width of the velocity distribution, can be extracted.

To understand how it is possible for a solitary wave to form in the granular bed Chapter 4 presents a different theoretical approach. Here one tries to establish a simple model for the evolution of the local bed thickness in the annular channel rather than detailed knowledge about the dynamics of individual particles. Therefore a set of two partial differential equations for the local bed thickness was established in analogy to continuum models of traffic flow that were able to reproduce "phantom jams" i.e. traffic jams that spontaneously appear out of homogeneous flow when the car density lies above a critical density. The experimentally determined local flow velocity as function of bed thickness goes as input into these equations. Experimental observations were also used to fix the equations' parameters. From this model the stability region for homogeneous flow can be determined. Moreover, once a model has been established, numerical simulations give a prediction of how any given initial material distribution evolves.

An effort to model extended pattern formation of vibrotransported granulate is currently being undertaken by the theory group in Münster using a continuum approach.

In the experiments with the annular vibration apparatus it was noted that transport properties are highly dependent on the state of fluidization. That is how interest arose for the way a granular packing fluidizes and how the fluidization transition is influenced by the parameters of the driving as well as particle size and material. To answer all these questions and characterize the various states of the system it is necessary to detect and track individual particles. Therefore a two-dimensional system was chosen. In that case all particles are visually accessible all of the time and particle positions can be determined from digital images taken by a single high speed camera. The experiments presented in Chapter 7 were done using a vertically oscillated square container.

In the next two chapters the setups for the experiments in the annular vibration apparatus and the vertical shaker are described. In Chapter 3 results of investigations into the phenomenon of extended surface waves are presented, followed by a description of localized surface waves in Chapter 4. The sublimation of a granular monolayer is reported in Chapter 5. Finally Chapter 7 treats the granular meltdown of a vertically vibrated, two-dimensional packing. The last chapter gives some final concluding remarks together with an outlook on remaining problems and open questions to be addressed in future experiments and simulations.

Chapter 2

Setup for circularly vibrated granular beds

Because of the dissipative nature of particle collisions, in order to maintain a steady flow or a dynamic steady state energy has to be fed constantly into a granular system. In lab experiments this is often done by applying a sinusoidal horizontal or vertical oscillation to the container. One of the aims of this work was to study effects of the combined action of both forms of agitation. In industry, troughs or plates vibrating in an inclined direction, so-called vibratory conveyors, are widely used to transport material. Choosing a ring-shaped container geometry, the long-time dynamics of a closed, mass conserving system devoid of disturbances from the influx and outpouring of grains can be studied.

In the following, the mechanics of the driving unit that excites the container oscillation is presented. As a start the excitation principle for a simple linear oscillation is explained. A linear sinusoidal vibration of a mass M_0 suspended with springs of stiffness k to a fixed support is achieved by two counterrotating unbalanced rotors of mass m_u. A rotor is unbalanced if its center of rotation does not coincide with the center of mass. The rotation frequency be f. Energy loss in the springs is assumed to be due to viscous damping with damping coefficient c. The system is illustrated in Fig. 2.1. A revolving mass dm at position $\vec{e}$ with respect to its center of rotation exerts a force $d\vec{f} = \frac{\partial^2}{\partial t^2}\vec{e}\,dm = (2\pi f)^2\ \vec{e}\,dm$ on M_0. The reflection symmetry in the arrangement and motion of the two rotors leads to a cancellation of all horizontal forces. Thus the trajectory of M_0 is constrained to vertical excursions y from the equilibrium position. The equation of motion for the system of masses reads

$$-ky - c\frac{\partial y}{\partial t} = M_0\frac{\partial^2 y}{\partial t^2} + 2\int_{m_\mathrm{u}} \frac{\partial^2}{\partial t^2}\left(y + e_v\right) dm \quad , \tag{2.1}$$

where e_v is the vertical component of $\vec{e}$ and one integrates the vis inertiae of all mass

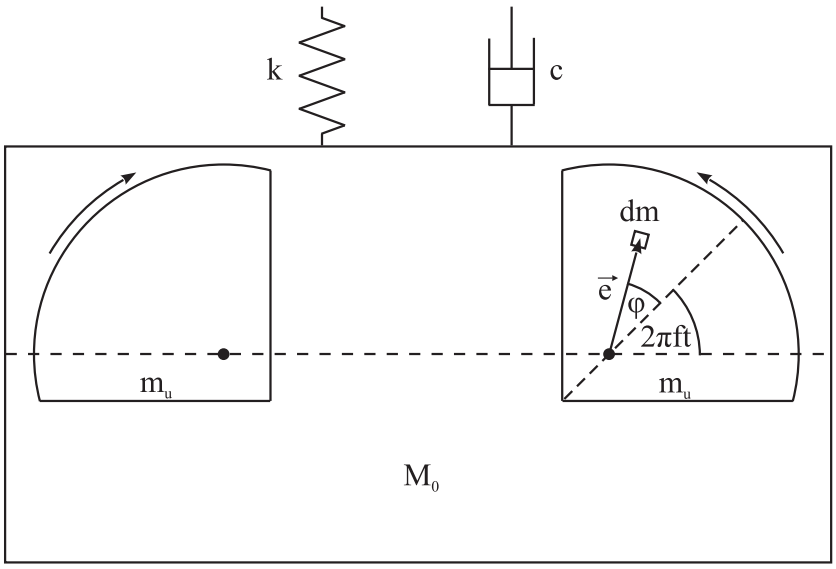

Figure 2.1: sketch of the driving

elements of one of the rotors. This can also be written as

$$M_{\mathrm{tot}}\frac{\partial^2 y}{\partial t^2} + c\frac{\partial y}{\partial t} + ky = -2\frac{\partial^2}{\partial t^2}\int_{m_\mathrm{u}} e_v\, dm \quad , \tag{2.2}$$

with $M_{\mathrm{tot}} = M_0 + 2m_\mathrm{u}$. If the unbalanced masses are plates of homogeneous thickness with vertical cross sections S the integration over the mass elements dm can be substituted by an integration over their vertical cross sections da as follows:

$$\int_{m_\mathrm{u}} e_v dm = \frac{m_\mathrm{u}}{S}\int_S e_v da = \frac{m_\mathrm{u}}{S}\int_S |\vec{e}|\sin(\varphi + 2\pi f t)\, da = m_\mathrm{u}\left[\frac{1}{S}\int_S |\vec{e}|\cos\varphi\, da\right]\sin(2\pi f t) \quad , \tag{2.3}$$

where φ is the angle enclosed by $\vec{e}$ and the rotor's axis of symmetry (see Fig. 2.1). The term in square brackets can be interpreted the effective eccentricity e_{eff} of the unbalance. Inserting Eq. 2.3 into Eq. 2.2 gives

$$M_{\mathrm{tot}}\frac{\partial^2 y}{\partial t^2} + c\frac{\partial y}{\partial t} + ky = 2m_\mathrm{u}(2\pi f)^2 e_{\mathrm{eff}}\sin(2\pi f t) \quad , \tag{2.4}$$

the equation of motion for a damped forced oscillator. Its solution is given by

$$y = A\sin(2\pi f t - \alpha) \quad , \tag{2.5}$$

where

$$A = A_t\frac{f^2}{\sqrt{\left(f_0^2 - f^2\right)^2 + \left(2\xi f_0 f\right)^2}} \tag{2.6}$$

with the resonant frequency $f_0 = \frac{1}{2\pi}\sqrt{\frac{k}{M_{\mathrm{tot}}}}$, the terminal amplitude $A_t = e_{\mathrm{eff}} 2\frac{m_\mathrm{u}}{M_{\mathrm{tot}}}$ and the damping ratio $\xi = \frac{c}{2\sqrt{kM_{\mathrm{tot}}}}$. The experimental apparatus was designed to operate

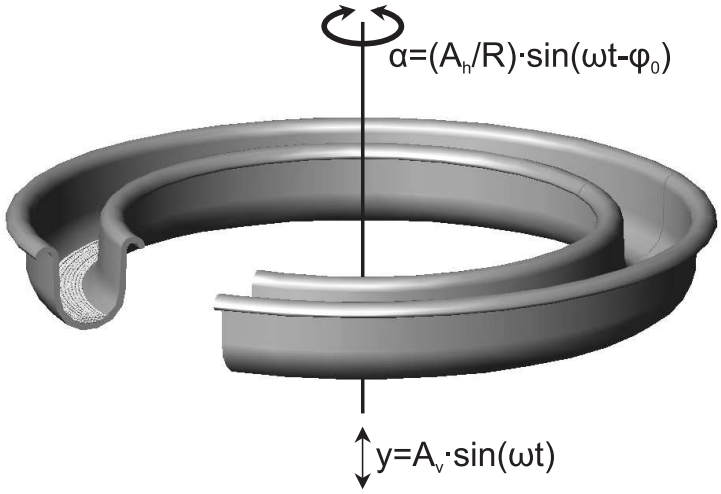

Figure 2.2: Geometry of the ring shaped container and its movement. An angular and a vertical vibration are superposed with a phase shift of $\pi/2$.

well above the resonant frequency, where the response amplitude A approaches A_t. In Section 2.1 Eq. 2.6 is fitted to the measured vertical response amplitude, delivering the values of e_{eff}, k, and c for the vertical oscillation.

For the experiments described in Chapter 3 a torus-shaped, 5 cm wide trough of light-wight, carbon fiber strengthened epoxy was used as particle container. The ring radius was $R = 22.5\,\text{cm}$ resulting in a circumference $L = 141\,\text{cm}$ (see Figure 2.2). In the subsequent experiments of Chapters 4 and 5 the granular material was contained in a 2 cm wide and 7 cm high annular channel with the same radius. The side walls of the new container were made of transparent Plexiglas mounted on a stainless steel floor. All experiments were conducted with open top under ambient atmosphere. Grounding the floor and working at elevated relative humidity ($> 50\,\%$) kept electrostatic charges negligible and led to reproducible results.

The channel was firmly connected to four symmetrically arranged driving units which are suspended with elastic bands in a highly adjustable frame (see Fig. 2.3). The driving units are coupled to an electric motor (SIEMENS Combimaster 1UA7) via a central gear box with drive shafts equipped with compensation clutches (see Fig. 2.4). As demonstrated before, two counter rotating unbalanced masses cause a linear vibration. Each driving unit consists of two synchronously acting linear vibrators, oriented perpendicular to one another. The trajectory a point in the center of the container follows is determined by the phase shift between the horizontal and the vertical oscillations and their amplitudes. In principle any trajectory from linear through elliptical to circular can be produced (see Fig. 2.4b). The phase shift is set through the choice of angle at which the unbalanced masses are mounted (Grochowski et al. 2004; Rouijaa et al. 2005). The vibration

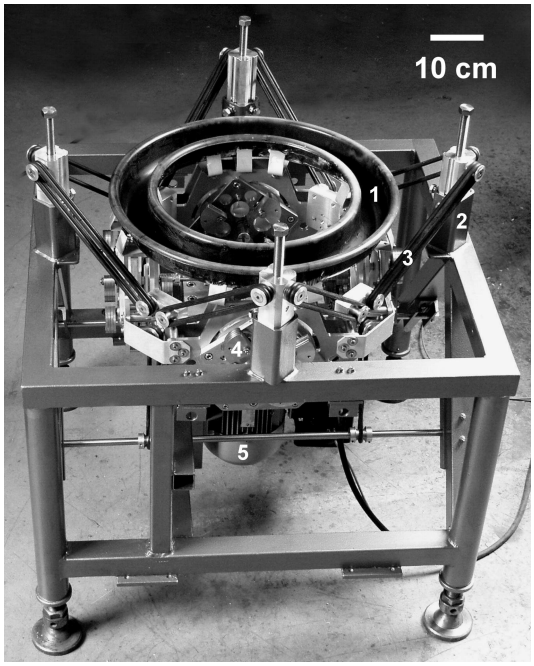

Figure 2.3: Annular conveyor: (1) torus-shaped vibration channel, (2) adjustable support, (3) elastic band, (4) vibration module with unbalanced masses, (5) electric motor with integrated frequency inverter.

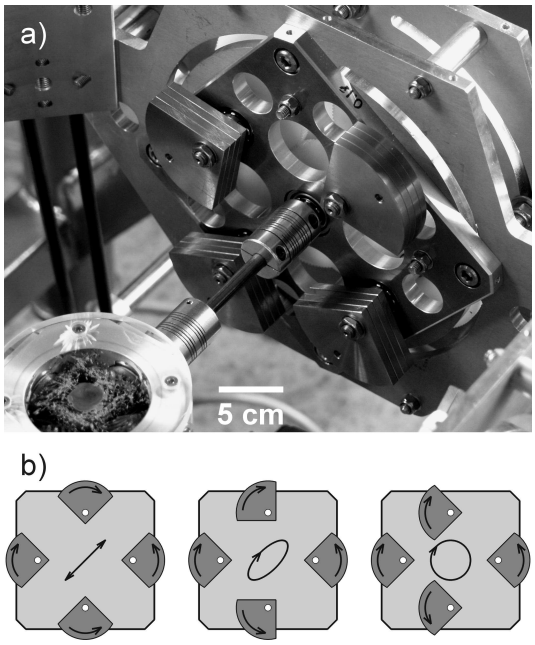

Figure 2.4: a) Driving module with four unbalanced masses; b) principle modes of oscillation: linear, elliptic, circular

amplitude at frequencies well above the resonant frequency is adjusted by varying the rotor plate thickness, thus changing m_u which enters the formula for the terminal amplitude $A_t = e_\mathrm{eff} 2\frac{m_\mathrm{u}}{M_\mathrm{tot}}$. The driving frequency could be adjusted on a control panel provided with the motor. The highest attainable frequency is about 30 Hz. A reflection sensor placed in front of a disc that bears a reflecting sticker and that is attached to one of the rotors served to measure the frequency. Each time the sticker passes by the reflection sensor sends out a rectangular voltage pulse. Its repetition rate was monitored on an oscilloscope (TDS 210) to an accuracy of 2 %.
The granular material was thus agitated by vertical sinusoidal oscillations of the container $y(t) = A_\mathrm{v} \sin(2\pi f t)$. Additionally the ring performed a sinusoidal angular oscillation $\alpha(t) = (A_\mathrm{h}/R)\sin(2\pi f t - \varphi_0)$ around its axis of symmetry. For the presented experiments a combination of unbalanced masses was chosen such that $A_\mathrm{v} \approx A_\mathrm{h}$ and $\varphi_0 \approx \pi/2$ i.e. every point of the channel floor followed approximately a circular trajectory in a plane tangent to the ring. The actual values of A_v, A_h and φ_0 were measured for each set of unbalanced masses and each frequency by a method described in section 2.1.
In the transparent channel spherical basalt glass beads (density: 3.0 g/cm^3) with diameter $d = 1.18 \pm 0.03$ mm were used as model granular material. A densely packed monolayer of these particles consists of 21,500 beads. The experiments in the epoxy trough were all done at a filling of 466,000 spherical lime glass beads (density: 2.3 g/cm^3) with a diameter of 1.11 ± 0.04 mm. In a close packing this number of particles would result in a filling height of 11.0 mm or 13.4 particle layers above the trough bottom.

2.1 Determination of the container motion

The suspended mass M_tot is actuated by four driving units with two horizontal rotor pairs each. According to Eqs. 2.5 and 2.6 its vertical displacement is sinusoidal with an amplitude A_v of

$$A_v = A_{t,v} \cdot \frac{f^2}{\sqrt{\left(f_{0,v}^2 - f^2\right)^2 + (2\xi_v f_{0,v} f)^2}} \quad , \tag{2.7}$$

where parameters of the vertical oscillation carry the subscript v to distinguish them from the parameters corresponding to the horizontal angular oscillation marked in the following with the subscript h. The resonant frequency $f_{0,v} = \frac{1}{2\pi}\sqrt{\frac{k_v}{M_\mathrm{tot}}}$ depends on the spring constant for displacements in the vertical direction k_v. The damping ratio $\xi_v = \frac{c_v}{2\sqrt{k_v M_\mathrm{tot}}}$ is proportional to the damping constant in the vertical direction c_v. In contrast, the terminal amplitude $A_{t,v} = e_\mathrm{eff} 16\frac{m_\mathrm{u}}{M_\mathrm{tot}}$ is independent of the spring characteristics.
To preserve rotation symmetry, in the horizontal plane the container performs an angular oscillation around its axis of symmetry. The excursion angle α from the equilibrium

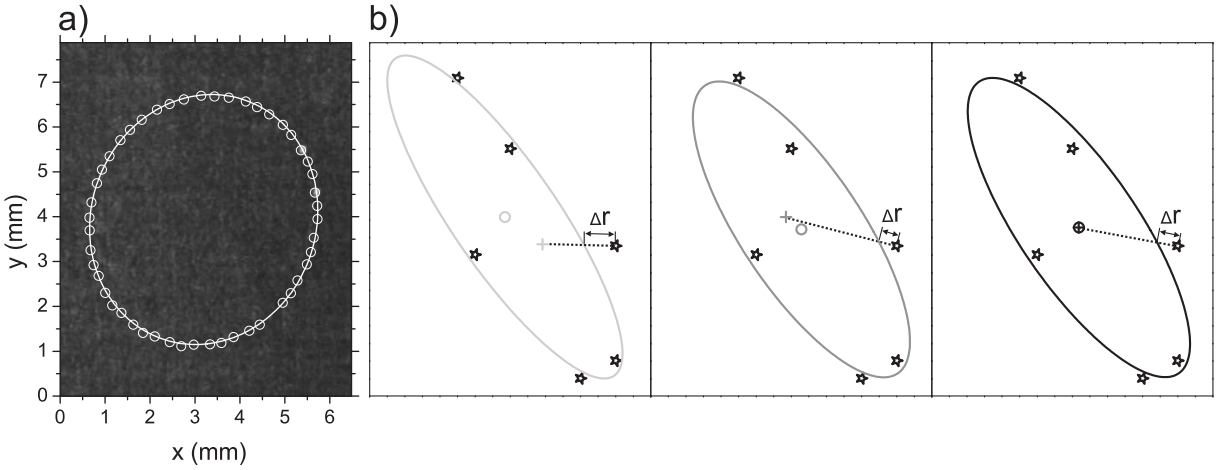

Figure 2.5: a) Detected positions (circles) of a bright revolving spot ($f = 7.33\,\mathrm{Hz}$, $m_\mathrm{u} = 243\,\mathrm{g}$). The line is an ellipse fitted to the data. b) Example of the fitting procedure. From left to right the images show the first, second and third fit to the data points (stars). Crosses are the reference points and circles mark the centers of the fitted ellipses.

position satisfies the equation of motion

$$I_\mathrm{tot}\frac{\partial^2\alpha}{\partial t^2} + c_\alpha\frac{\partial\alpha}{\partial t} + k_\alpha\alpha = \frac{I_u\,(2\pi f)^2\,e_\mathrm{eff}}{R}\sin(\omega t) \quad , \tag{2.8}$$

where I_tot denotes the total moment of inertia of the suspended mass, I_u the moment of inertia of the vertical rotor pairs and R the mean container radius. Once again the solution is a sinusoidal oscillation. Its amplitude be A_α. Then the horizontal amplitude in the center of the container A_h is given by

$$A_h = RA_\alpha = A_{t,h}\frac{f^2}{\sqrt{\left(f_{0,h}^2 - f^2\right)^2 + \left(2\xi_h f_{0,h} f\right)^2}} \tag{2.9}$$

with the resonant frequency $f_{0,h} = \sqrt{\frac{k_h}{I_\mathrm{tot}}}$, the terminal amplitude $A_{t,h} = e_\mathrm{eff}\frac{I_\mathrm{u}}{I_\mathrm{tot}}$ and the damping ratio $\xi_h = \frac{c_h}{2\sqrt{k_h I_\mathrm{tot}}}$.

Horizontal and vertical rotor pairs of equal mass were mounted to oscillate with a phase shift of $\pi/2$. Because the total suspended mass and the unbalanced masses are distributed over R — the distance to the symmetry axis of the container — in a similar way $\frac{I_\mathrm{u}}{I_\mathrm{tot}} \approx \frac{16m_\mathrm{u}}{M_\mathrm{tot}}$. Since the main springs are oriented at an angle of 45° to the vertical direction, $k_h \approx k_v$ and $c_h \approx c_v$. Thus a roughly circular motion is expected in the middle of the channel which contains the granulate.

The actual phase shift between horizontal and vertical oscillation as well as the oscillation amplitudes in both directions were determined from the shape of the trajectory drawn by a mark on the container. A bright spot on dark background attached to the outer container

m_u (g)	$A_{t,v}$ (mm)	f_0 (Hz)	ξ
128	1.410 ± 0.003	3.59 ± 0.02	0.069 ± 0.015
162	1.71	3.52	0.068
209	2.09	3.42	0.066

Table 2.1: The values given for $m_\mathrm{u} = 128\,\mathrm{g}$ are fit results . The rest has been calculated from the model using these results.

wall was stroboscopically illuminated and filmed by a CCD camera at a frequency of 60 Hz. Since the stroboscope frequency was two to three times the camera frequency images were exposed several times (see background image in Fig. 2.5a.
The images, stored as bitmaps $b_{i,j}$, were correlated with a pyramidal brightness pattern $p_{k,l}$, the size N of which was compable to the size of the bright spots in the image,

$$p_{k,l} = \min\left\{1 - \left|\frac{2k}{N-1}\right|, 1 - \left|\frac{2l}{N-1}\right|\right\} \quad ,$$

where

$$k, l \in \left\{\frac{1-N}{2}, \frac{1-N}{2} + 1, \ldots, \frac{N-1}{2}\right\} \quad \text{, and } N \text{ is odd.}$$

The correlation matrix $c_{i,j}$, calculated according to

$$c_{i,j} = \sum_{k,l=\frac{1-N}{2}}^{\frac{N-1}{2}} b_{i+k,j+l} \cdot p_{k,l} \quad ,$$

then had its most intense local maxima at the spot positions. Subpixel resolution was achieved by parabolic interpolation around the detected local maxima.
The open circles in Fig. 2.5a indicate the spot positions extracted from 25 images. The superposition of two sinusoidal oscillations of equal frequency results in an ellipse. The length of its major and minor axis and the tilt of the major axis with respect to the horizontal are uniquely connected to the oscillation amplitudes and the phase shift between the oscillations.
An ellipse is fitted to the data in a way to minimize the sum of deviations between data points and ellipse. The deviation between a data point and the ellipse is measured along a line through the data point and a reference point. Initially the center of mass of the data points is taken as reference point. In a next iteration the center of the previously fitted ellipse becomes the new reference point and so on. With this procedure the center of the fitted ellipse and the reference point converge. The fitting routine is stopped once the distance between old and new reference points falls below 1/100 pixel. Fig. 2.5b illustrates the method.

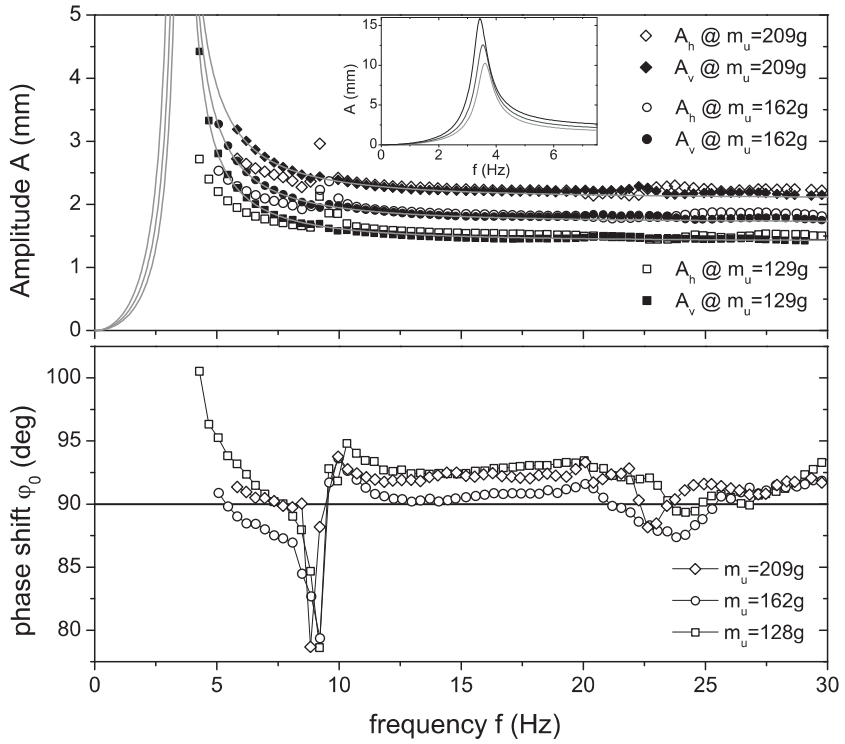

Figure 2.6: Frequency response of the system with epoxi trough. The inset in the upper graph shows the behavior of the theory curves around the resonance.

Extensive studies of the container motion have been conducted with the torus shaped epoxy trough. The values obtained for the vertical and horizontal oscillation amplitudes at the center of the container, A_v and A_h respectively, and the phase shift φ_0 at various frequencies and for several unbalanced masses are shown in Fig. 2.6. Data were acquired for frequencies from just above the main resonant frequency up to the highest frequencies achievable with the apparatus. The horizontal resonance occurs at lower frequencies than the vertical resonance, indicating that the spring constant for horizontal excursions from the equilibrium position is smaller than the spring constant for the vertical motion. There is an additional minor resonance at about 8 Hz, which is associated with some nonuniform oscillation mode. At the resonances the phase shift deviates significantly from the 90°, expected for circular vibration. Above 10 Hz these deviations fall below 5 %. In this range the amplitudes in the vertical and horizontal directions are very close to one another and with increasing frequency they approach a constant value. This is where the experiments described in the following chapters were conducted. Mounting more unbalanced mass m_u basically shifts the curves towards higher amplitudes.

According to Eqs. 2.7 and 2.9 the frequency response is characterized by three parameters, namely the terminal amplitude A_t, the resonant frequency f_0 and the damping rate ξ. For the vertical oscillation caused by unbalances of $m_\mathrm{u} = 129\,\mathrm{g}$ these parameters were

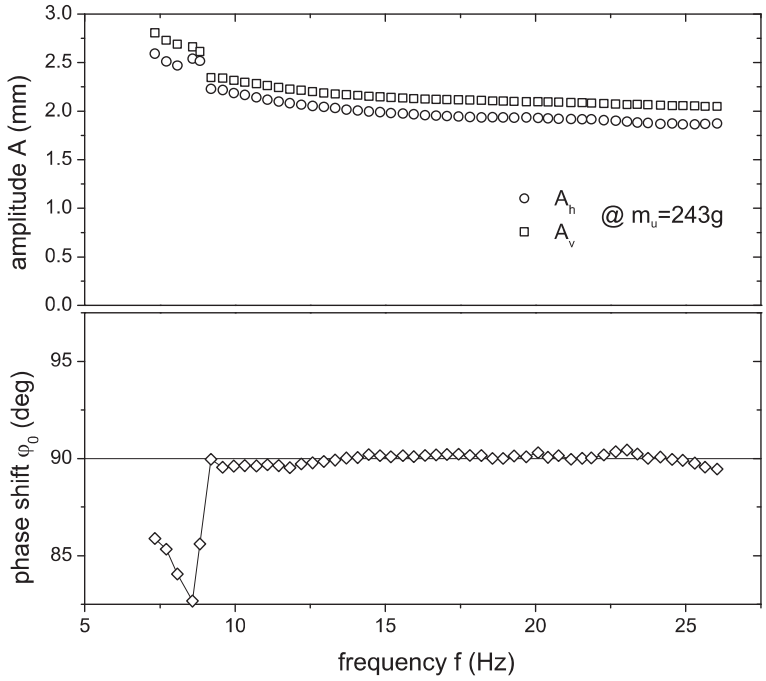

Figure 2.7: Frequency response of the system with Plexiglas container.

determined by fitting model Eq. 2.7 to the data. From the results shown in Table 2.1 effective eccentricity e_{eff}, spring constant k_v, and damping coefficient c_v can be calculated after the suspended mass without rotors has been weighed ($M_0 = 22.0\,\text{kg}$). One obtains $e_{\text{eff}} = 17.94\,\text{mm}$, $k_v = 132.6\,\text{N/cm}$, and $c_v = 81.12\,\text{kg/s}$. Now $A_{t,v}$, $f_{0,v}$, and ξ_v can also be specified for the other examined unbalanced masses $m_{\text{u}} = 162\,\text{g}$ and $m_{\text{u}} = 209\,\text{g}$ (see Table 2.1). The theoretically expected frequency response drawn in Fig. 2.6 is in excellent agreement with the measured data.

With mounted Plexiglas container the suspended mass was $M_0 = 27.3\,\text{kg}$. To set it in motion unbalances of 243 g were used which produced the frequency response depicted in Fig. 2.7. The fact that the amplitude of the vertical oscillation was always higher than the amplitude of the horizontal oscillation is explained by the geometry of the container mounting. The suspended mass was distributed around the distance R from the symmetry axis such that $\frac{I_{\text{u}}}{I_{\text{tot}}} < \frac{16 m_{\text{u}}}{M_{\text{tot}}}$ and therefore $A_{t,h} < A_{t,v}$. Above the minor resonance, again to be observed around 8 Hz, the phase shift φ_0 was 90° to within 2 % and the difference between vertical and horizontal amplitude was smaller than 0.2 mm.

2.2 Imaging

For the examination of the extended surface waves described in Chapter 3 the transparent container was not yet available. The used epoxy trough only allowed to monitor the

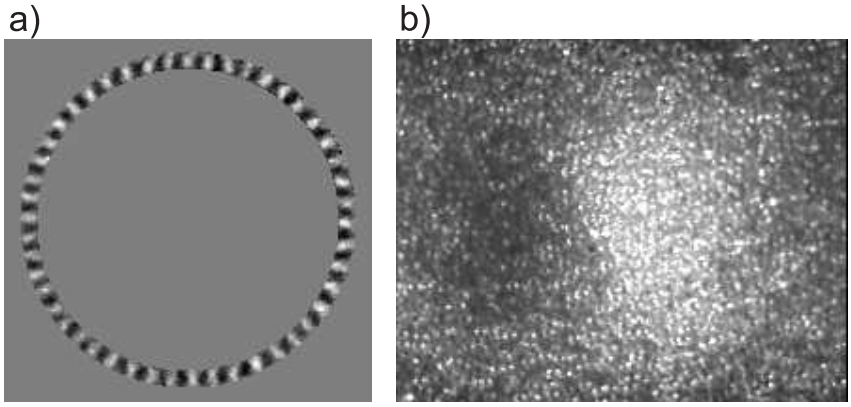

Figure 2.8: a) Top view of granular surface waves in the annular trough. b) Close up. The width of the image corresponds to a length of 3.3 cm

granular bed from the top. To visualize surface undulations the granulate was lighted under small angle with respect to the surface by 18 goose neck glass fibre light guides connected to 6 cold light sources. In a top view, peaks then shone brightly, while valleys lay in the dark. As an example Fig. 2.8a shows the granular surface wave pattern that arises at a driving frequency of 23.8 Hz with unbalances of 162 g. To eliminate brightness variations due to inhomogeneous illumination the gray value of each pixel was divided by the mean gray value of that pixel, calculated from a sequence of images spanning many forcing cycles. In the close up snapshot Fig. 2.8b, taken at a driving frequency of 22.3 Hz with unbalances of 128 g, even individual particles can be distinguished. Images were taken with a Kodak Ektapro high speed digital imaging system with a resolution of 239×192 pixel at rates of up to 1000 images per second.

The granular material in the Plexiglas channel was lit through diffusive parchment paper wrapped around the outer wall, using the same light sources as for the setup with the epoxy trough. Hence, through the inner channel wall particles appear dark in front of a bright background. The granular bed was observed from the top via a conical mirror placed in the center of the ring, like in the experiments of van Doorn and Behringer (1997) (see Fig. 2.9). Thus a side view of the whole channel was captured with a single high-speed digital camera (Redlake MotionPro 500). The image resolution was 1280×1024 pixels at rates up to 500 images per second. Fig. 2.10a shows the granular bed as seen by the camera in the conical mirror. Unfolding these mirror images delivers 360° panoramic side views of the granular profile in the channel as presented in Fig. 2.10b. In order to eliminate brightness variations due to inhomogeneous illumination the gray value of each pixel is devided by the mean gray value of that pixel when the empty container is filmed. To enhance the image contrast the brightness scale is linearly streched and shifted such that the minimum gray value is 0 and the maximum is 255 (see Fig. 2.10c).

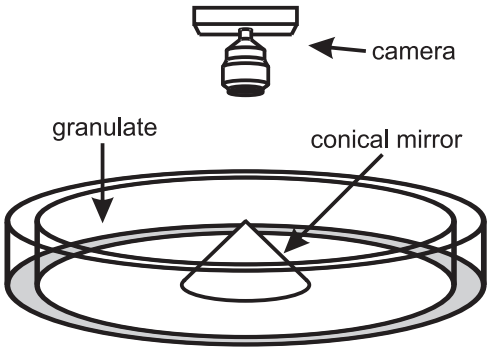

Figure 2.9: Geometry of the container and imaging system.

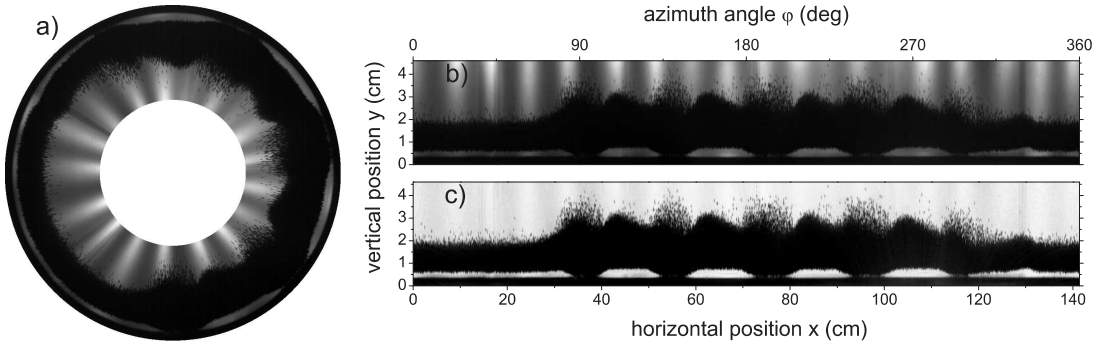

Figure 2.10: Unfolding of the captured images.

The unfolding operation transforms a ring-shaped mirror image into a rectangular side view of the channel, where the horizontal position indicates the azimuth angle and the vertical position corresponds to height. For the conversion the picture elements of the mirror image are attributed to sectors according to their distance from the mirror center and their angle to the horizontal with respect to the mirror center as shown in Fig. 2.11a. The width and height of the bitmap created to hold the transformed image (Fig. 2.11b) are equal to the number of angular segments and the number of radial subdivisions, respectively. The arithmetic mean of the brightness of all pixel belonging to a sector is then mapped to the corresponding pixel of the bitmap.

The camera can also be triggered externally for stroboscopic recordings. To acquire one image per forcing cycle at a fixed phase of the driving the electro-optical triggering system employed to measure the driving frequency was used. The output signal then serves as trigger input for the high speed camera system.

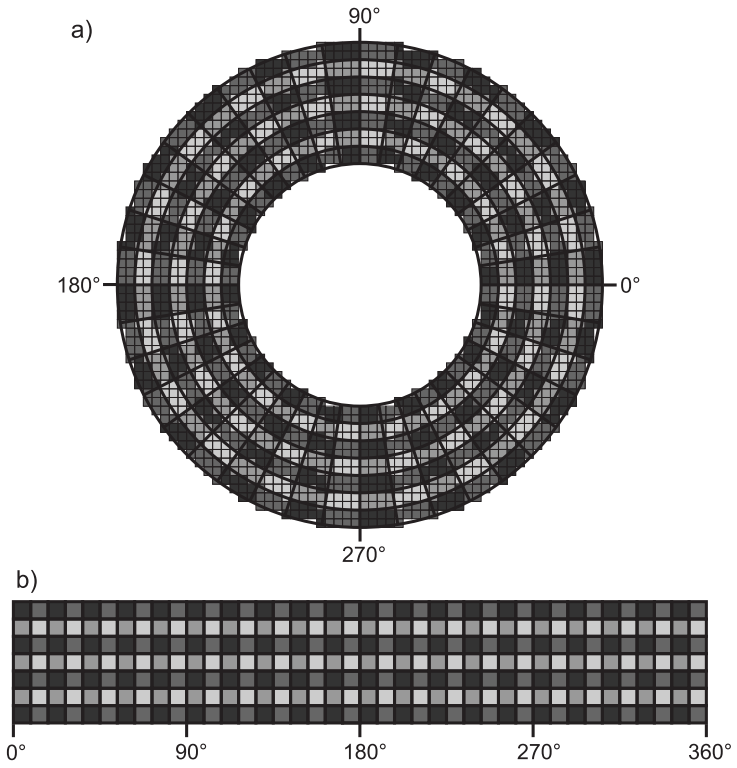

Figure 2.11: Unfolding the mirror images. The thin rectangular grid in a) divides the artificial mirror image into its picture elements. Thick lines in a) enclose the segments used for the conversion. The grid in b) visualizes the bitmap created to hold the transformed image.

Chapter 3

Extended surface waves

Extended surface patterns were examined in the epoxy trough mounted on the annular vibration apparatus. The granular material was agitated by a superposition of vertical and horizontal vibrations of equal amplitudes and a phase shift of $\pi/2$. That means that every point of the support followed a circular trajectory. Standing waves oscillating at half the forcing frequency were observed within a certain range of the driving acceleration. The dominant wavelength of the pattern was measured for various forcing frequencies at constant amplitude. These waves are not stationary, but drift with a velocity equal to the transport velocity of the granular material, determined by means of a tracer particle. The research work presented in this chapter has been published in the proceedings of the conference "Powders and Grains 2005" that took place in Stuttgart (Götzendorfer et al. 2005).

3.1 Introduction

Providing a granular material with energy can make it behave like a liquid. One example are avalanches. The energy that particles gain when sliding down a steep slope leads to the fluidization of large parts of the granular surface. Another example are surface waves in vibrated beds. When a layer of granular material is repeatedly kicked by an oscillating support, surface waves are excited that resemble Faraday waves known from thin layers of shaken liquids. The mechanism responsible for this granular pattern formation is not yet fully clear. What complicates the situation is that the type of the wave is probably not the same throughout the whole range of driving parameters and particle sizes over which the phenomenon has been observed. Metcalf et al. (1997) and Umbanhowar and Swinney (2000) pointed out that at low driving frequencies small particles travel half a wavelength during each forcing cycle, and patterns result from a sloshing back and forth motion of the granular material. In contrast, for high forcing frequency and big particles

the movement of the individual grains is reported to be more random in character, and the horizontal mobility is estimated to be very low. Then one deals either with bending waves or density waves. It will be demonstrated that the experiments presented here concern the latter regime.

Clément et al. (1996) and Wassgren et al. (1997) investigated granular surface waves in vertically oscillated two-dimensional or quasi two-dimensional beds in rectangular containers. Pattern formation in cylindrical containers upon vertical oscillation was examined by Melo et al. (1994, 1995), Umbanhowar and Swinney (2000) and Metcalf et al. (1997). The experiments presented here differ from the above mentioned by the ring shaped geometry of the container and an additional horizontal shaking component. The cited two-dimensional and quasi two-dimensional experiments work with containers that have a relatively low bed height/container length ratio of about 1/10 to 1/15. When filled up until the number of particle layers is comparable to that present in the experiments reported in this chapter very few waves fit into these boxes. In contrast, the circumference of the annular container is 130 times larger than the bed height. This is enough to accommodate 27 waves of the longest observed wavelength. When driving parameters were such that the wavelength was shortest more than 60 waves were counted in the ring. The combination of angular and vertical container oscillation breaks the reflection symmetry of the system and results in material transport (Grochowski et al. 2004; Rouijaa et al. 2005). The influence of the additional horizontal oscillation component on the wave pattern has not been studied before.

3.2 Experiment

For the experiments presented in this chapter we used 466,000 spherical glass beads with a diameter of 1.11 ± 0.04 mm which were contained in the ring-shaped epoxy trough. In a close packing this number of particles would result in a filling height of 11.0 mm or 13.4 particle layers above the trough bottom. The shaking amplitude both in the vertical and the horizontal directions was kept constant at $A = 1.47$ mm, with a standard deviation of 0.03 mm or 2 %. The phase difference between the two vibration components was fixed at $\pi/2$. A detailed description of the experimental setup is given in Chapter 2.

3.3 Results and Discussion

From earlier research into the transport properties of granular material upon circular shaking (Grochowski et al. 2004; Rouijaa et al. 2005) it is known that the most important forcing parameter is the normalized maximum acceleration $\Gamma = A\omega^2/g$, where ω is

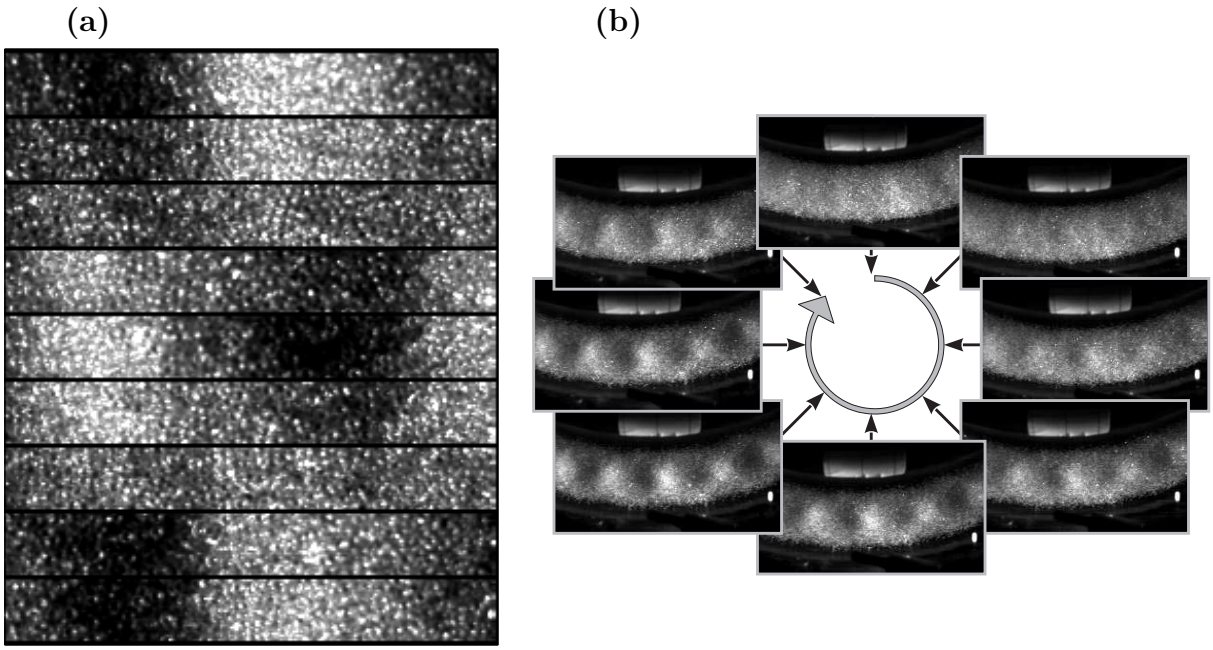

Figure 3.1: The surface of the granular bed in close-up snapshots for a normalized peak forcing acceleration $\Gamma = 3.00$ at $f = 22.3\,\mathrm{Hz}$ driving frequency. In (a) time increases from top to bottom by 12 ms, corresponding to 0.27 driving periods, between successive images. The length of the stacked stripes is 3.3 cm. In (b) the evolution of the surface topography over one forcing cycle is tracked. The circle in the center indicates the trajectory of the support. The image width is 14 cm.

the angular driving frequency and g the gravitational acceleration. In the experiments presented here standing surface waves oscillating at half the driving frequency were found in the range $20\,\mathrm{Hz} < f < 29\,\mathrm{Hz}$. Using measured values for the driving amplitudes the corresponding acceleration Γ was calculated to lie in the interval $2.4 < \Gamma < 4.8$. At Γ below 2.4 the granular surface was flat. This was also true for Γ above 4.8, but here the layer flight time exceeded the forcing period, and kink type defects appeared between regions oscillating out of phase.

Figure 3.1 shows series of close-ups of the granular surface at $\Gamma = 3.0$. The evolution of the surface wave during a forcing cycle was analyzed with the help of films taken at 1000 frames per second. The wave amplitude is highest after the support has passed its lowest position and accelerates upward. Then the wave amplitude decays, and the surface becomes eventually completely flat, when the container has passed its maximum position and accelerates downward. In the following half cycle, a wave builds up again with peaks at positions where before were valleys and vice versa. Its amplitude grows until it reaches a maximum and the cycle starts anew.

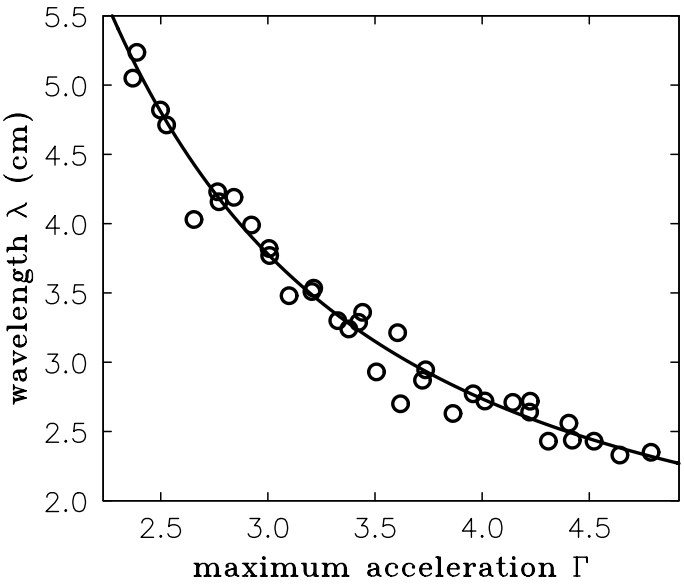

Figure 3.2: Circles represent the measured wavelength λ plotted over the normalized acceleration Γ. Throughout the measurement the driving amplitude was kept constant at 1.47 mm. The solid line is the graph of the function $\lambda = 1.3\,\mathrm{cm} + 20\,\mathrm{cm} \cdot \Gamma^{-1.9}$, the best fit to the data.

3.3.1 Wavelength

In order to monitor the pattern dynamics, images were taken only once per forcing cycle, when the wave was at maximum amplitude. The fact that the waves are always oriented perpendicular to the side walls reduces the pattern to one dimension. Therefore the brightness along the circumference of the ring was evaluated by averaging over the width of the trough. The ring circumference was subdivided into bins of 1.4 mm length. In order to reduce effects of inhomogeneous illumination, for all images and each bin its time average was subtracted. Short wavelength fluctuations were eliminated by the application of a Gaussian filter (see Jähne 2002) with a standard deviation of 2.3 bins. A search for extrema yielded the peak and valley positions of the surface wave. The probability distribution function of the distances between neighboring extrema shows a strong peak at the dominant wavelength. This analysis in real space was favored over an evaluation in Fourier space, since it is more robust with respect to local perturbations of the wave pattern.

Figure 3.2 is a plot of the measured wavelength as a function of acceleration Γ. The wavelength of the surface wave decreases from 5.2 cm at onset to 2.3 cm just before it vanishes. Assuming a power law dependence, and allowing for a cutoff at a minimum wavelength $\lambda_{\min}$ a function of the form

$$\lambda = \lambda_{\min} + c \cdot \Gamma^{p}$$

was fitted to the data. The best fit is drawn as a solid line in Figure 3.2. The resulting minimum wavelength $\lambda_{\min}$ is 1.3 ± 0.3 cm, which is approximately the depth of the granular layer. The values for the other parameters are $c = 20 \pm 4$ cm and $p = -1.9 \pm 0.3$.

How does this result compare to other published wavelength measurements? Umbanhowar and Swinney (2000) gave the most accurate formula describing the dispersion relation at constant acceleration $\Gamma = 3.0$ and low frequencies. It reads

$$\lambda/h = 1.0 + 1.1 \cdot \left(f\sqrt{h/g}\right)^{-1.32} \quad ,$$

where h is the filling height assuming a filling fraction of 58 %. Metcalf et al. (1997) additionally examined the dependence of the wavelength on the peak acceleration Γ at constant frequency. At low frequencies they found a slow increase in wavelength as the peak acceleration is raised. The situation is completely different at high frequencies, where a sharp drop of the wavelength for increasing Γ has been reported. Furthermore at fixed peak acceleration the wavelength depends only weakly upon frequency, if at all. The crossover between the low and high frequency regimes occurs when the peak container velocity $v = 2\pi f A$ passes the critical value $v_{\mathrm{gm}} \approx 3\sqrt{dg}$. Both Umbanhowar and Swinney (2000), and Metcalf et al. (1997) associated this crossover with a change in grain mobility. They noticed that for $v > v_{\mathrm{gm}}$ the whole granular material performs a horizontal sloshing motion, while for $v < v_{\mathrm{gm}}$ grains are essentially immobile in the horizontal direction. Note that

$$v < v_{\mathrm{gm}} \Leftrightarrow f < 3/(2\pi a)\sqrt{dg} \Leftrightarrow f > \Gamma/(6\pi)\sqrt{g/d}.$$

This means that in measurements where Γ is kept constant the immobile grain regime is situated at high frequencies, whereas in the experiments presented in this Chapter the same behavior is expected below the crossover frequency $f_{\mathrm{gm}} = v_{\mathrm{gm}}/2\pi A$. With the measured values of d and A, one obtains $f_{\mathrm{gm}} = 34$ Hz, which is well above the frequencies at which the experiment operates. In conclusion the surface waves examined here are not caused by a horizontal back and forth motion of the particles, but by either a bending of the layer or a spatial density modulation. In fact although the particles of the top layer are fluidized and perform jumps their movement seems to be random in character and not coupled to the wave motion. The dependence of the wavelength on Γ reported here is consistent with the results of Metcalf et al. (1997) in the immobile grain regime. Evidence for a saturation of the wavelength at high Γ in the immobile grain regime has been given by Clément et al. (1996). They found the wavelength to be constant over a wide range of f and Γ, taking on a value of about twice the layer depth, which is in reasonable accord with the results obtained from the model fit presented above.

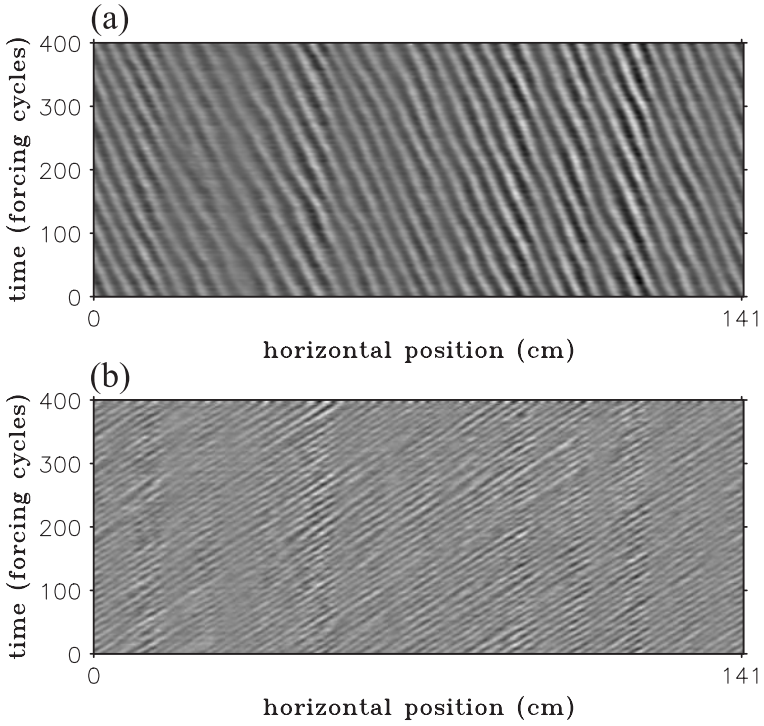

Figure 3.3: Space time plot showing the brightness of the granular surface at maximum wave amplitude every other forcing cycle for $\Gamma = 2.84$ (a) and $\Gamma = 4.22$ (b).

3.3.2 Drift velocity

The space-time-plots of Figures 3.3a, b display the surface brightness at maximum amplitude on every other cycle, accelerations Γ being 2.84 and 4.22, respectively. They demonstrate that the standing wave is drifting at constant velocity. The wave pattern is not exactly at the same position after two forcing cycles, but shifted a little to one or the other direction, depending on Γ. To obtain the drift velocity, the real space brightness data are Fourier transformed and the phase of the wave number belonging to the dominant wavelength is tracked. From the rate of phase change one is able to calculate the velocity of the pattern movement. Results are plotted in Figure 3.4 and compared to velocity measurements for a tracer particle that indicates the velocity of the surrounding material. As tracer particle serves a colored glass bead with a diameter of 6 mm, which is sufficiently large to prevent it from submerging, so that it remains visible all of the time. The drift velocity of the surface wave and the transport velocity of the granular material coincide. Worth mentioning is the fact that the surface waves disappear at the same value of Γ where the transport velocity starts to decrease.

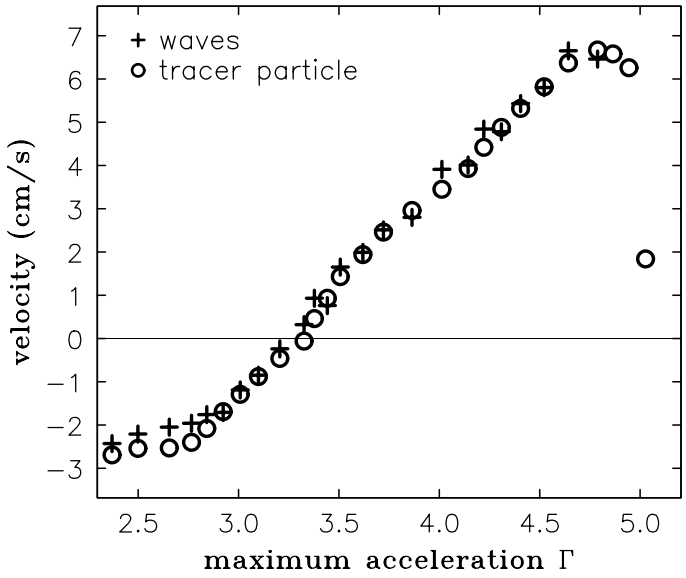

Figure 3.4: Measured velocity of a tracer particle (circles) and drift velocity of the surface waves (crosses) over the normalized acceleration Γ. Throughout the measurement the driving amplitude was kept constant at 1.47 mm.

3.4 Conclusion

In the framework of investigations into the phenomenon of granular surface waves upon circular oscillation of the container, the wavelength dependence on the forcing acceleration Γ was measured in the regime of low horizontal grain mobility. A drift of the standing wave pattern was found to occur, and the drift velocity matches the transport velocity of the granular material. Both velocities strongly depend on the forcing acceleration and even reverse sign at $\Gamma \approx 3.3$. The detected waves are similar to those seen in containers oscillating purely in the vertical direction. Obviously the horizontal oscillation component has little influence on the wave phenomenon, except for the drift.

When the experiments which are presented in this chapter were carried out, the transparent container was not yet available. A channel with Plexiglas walls later allowed to uncover the shape of the lower layer boundary during the flight phase (see Fig. 3.5). It turned out to be flat in the range $2.4 < \Gamma < 4.8$ and waves only showed up at the surface. In contrast, for a bending wave one would have expect arches underneath peaks of the surface undulations. Thus, if horizontal material displacement is ruled out the surface wave must be due to periodic lateral density variations. It would further be interesting to know the depth down to which the particle motion is affected by the surface wave and to have further information about the fluidization state of the granular bed. One could speculate that the wave motion is restricted to an upper fluidized part of the granular bed, while the lower part is in a solid-like state unaffected by the wave.

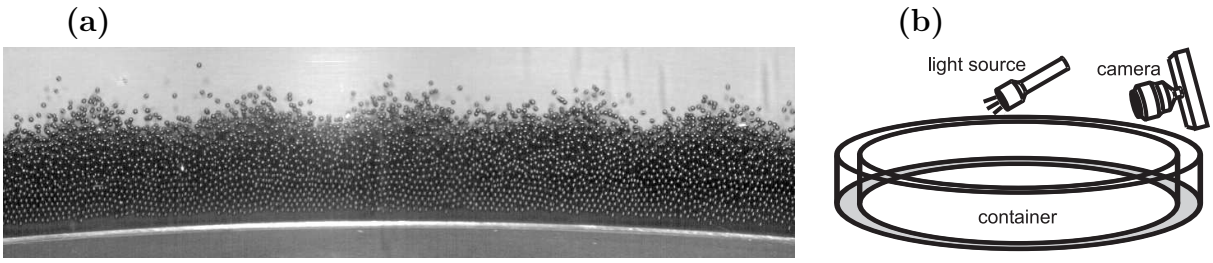

Figure 3.5: (a) Surface waves of a granular bed consisting of 8 particle layers for a normalized peak forcing acceleration $\Gamma \approx 3$ at $f \approx 20\,\mathrm{Hz}$ driving frequency. (b) Position of camera and lighting with respect to the Plexiglas container. As the particles are illuminated from the front they exhibit a bright reflection spot. The particle diameter is 1 mm.

For surface waves in purely vertically vibrated granular beds there exists a continuum model devised by Eggers and Riecke (2006) that reproduces experimenal results fairly well. In order to reproduce and explain the experimental data on circularly vibrated granular beds, presented here, Grevenstette and Linz (2006) generalized and modified this model. They used the following phenomenological equations to describe the spaciotemporal evolution of the local bed height $H(x,t)$ and the vertically averaged local flow velocity in the horizontal direction $v(x,t)$:

$$\begin{aligned} \frac{\partial H}{\partial t} + \frac{\partial\,(Hv)}{\partial x} &= D_1 \frac{\partial^2 H}{\partial x^2} \\ \frac{\partial v}{\partial t} + v\frac{\partial v}{\partial x} &= D_2 \frac{\partial^2 v}{\partial x^2} + f_h + f_v + f_d \end{aligned}$$

In these equations D_1 and D_2 are constants. The terms f_h and f_v contain the coupling of the granular bed to the horizontal and vertical driving components:

$$f_h = g\Gamma\cos(2\pi f t) \quad , \qquad f_v = -g\Gamma\sin(2\pi f t)\,\frac{\frac{\partial H}{\partial x}}{\sqrt{1+\left(\frac{\partial H}{\partial x}\right)^2}} \quad .$$

The term f_d accounts for the friction between granular material and container:

$$f_d = f_s - Bv \quad , \qquad f_s = \begin{cases} -\mu\,\mathrm{sgn}(v)\,a_N & \text{if} \quad a_N > 0 \\ 0 & \text{otherwise} \end{cases} \quad , \qquad a_N = g - g\Gamma\sin(2\pi f t) \quad ,$$

where μ and B are constants. Simulations of this model yield drifting subharmonic surface waves as found in the experiments. Yet in contrast to the experiments, in the simulations the wavelength increases with increasing forcing strength. Another shortcoming of the model is that it shows no reversal of the drift velocity.

Of some practical interest for industrial applications are the mixing properties in the surface wave regime. One might expect enhanced self diffusion in the presence of an undulated surface, compared to the state with a flat surface at lower and higher acceleration.

Chapter 4

Localized subharmonic waves

Localized period doubling waves arise in circularly shaken granular beds contained in an annular channel. These solitary wave packets are accompanied by a locally increased particle density. The width and velocity of the granular wave pulse were measured as a function of the bed height. A continuum model for the material distribution, based on the measured granular transport velocity as a function of the bed thickness, captures the essence of the experimental findings.
The simulations of the continuum model were conducted by Daniel Svenšek from the Department of Physics at the University of Ljubljana, who spent a year in Bayreuth as Humbold fellow working at the chair Theoretische Physik III.
The obtained results have been submitted for publication to Physical Review Letters (Götzendorfer et al. 2006).

4.1 Introduction

La Ola, the Mexican wave, investigated by Farkas et al. (2002), serves as a good illustration for solitary waves in annular systems. On a smaller scale, the confined state in binary mixture convection is a prime example of solitary waves in dissipative systems. These pulses of traveling waves, which appear in the neighborhood of a bistable regime, were experimentally investigated by Kolodner et al. (1988, 1991), Niemela et al. (1990), and Anderson and Behringer (1990). The physical mechanism behind the phenomenon was uncovered by Barten et al. (1991, 1995) and Jung and Lücke (2002), who solved the full hydrodynamic field equations. Riecke (1992) derived a set of amplitude equations to describe the self-trapping of traveling-wave pulses in these systems. The so-called "worms" in electroconvection, which were discovered by Dennin et al. (1996) and explained by Riecke and Granzow (1998), represent a different type of phenomenon in the sense that the associated bifurcation from the flat surface to extended traveling waves is

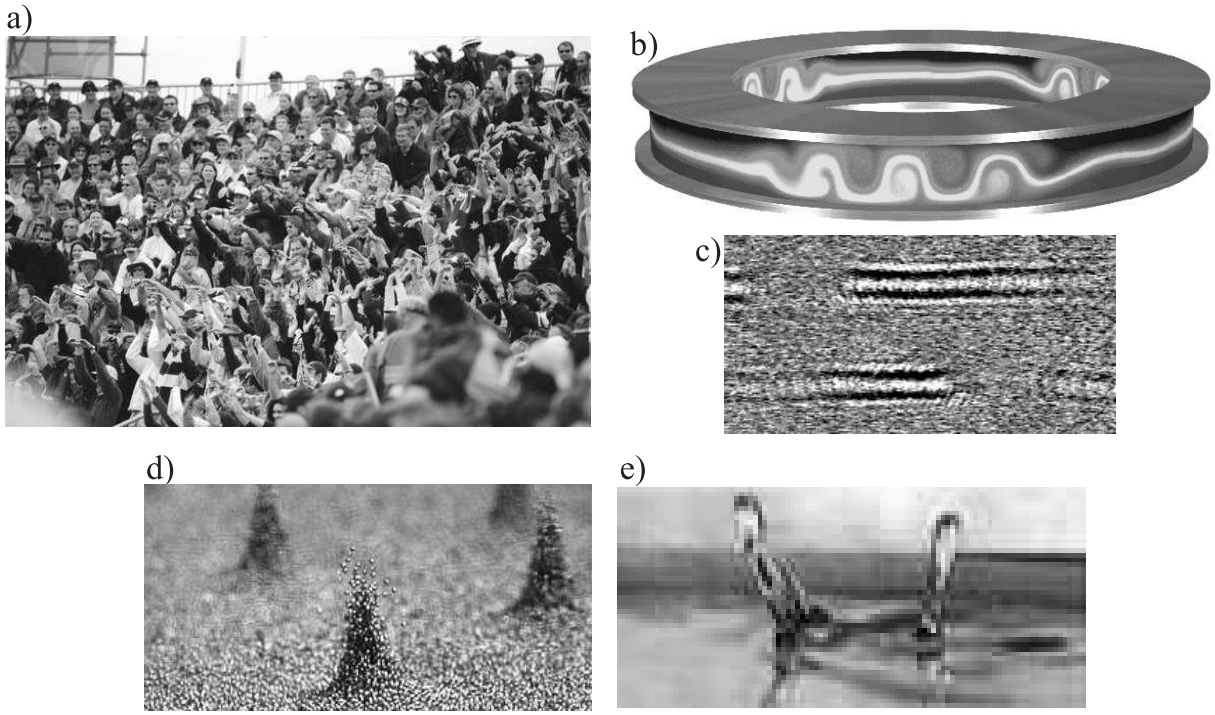

Figure 4.1: Solitary waves. (a) Mexican wave circulating in a sports stadium. (b) Confined state in a simulation of binary mixture convection (Image from `http://www.uni-saarland.de/fak7/luecke/main_de.html`). (c) "Worms" observed in electroconvection by Dennin et. al (1996). (d) Oscillons (Image from `http://chaos.ph.utexas.edu/research/granular.html`). (e) Propagating solitary state discovered by Lioubashevski et al. (1996).

supercritical. Moreover, periodically driven systems are known to exhibit highly localized stationary structures, coined oscillons (Umbanhowar et al. 1996), or propagating solitary waves with the periodicity of the driving (Lioubashevski et al. 1996, 1999). Fig. 4.1 shows examples of the mentioned solitary waves. Here we present drifting localized pulses that envelop parametrically driven, subharmonic, standing waves. They arise in a circularly vibrated granular bed. The results of our experiments are described by hydrodynamic equations.

4.2 Experiment

A detailed description of the experimental setup and the driving mechanism is given in Chapter 2. The vertical component of the container oscillation had an amplitude A_v of 2.06 mm at a frequency f of 26.0 Hz. From these values the normalized peak container acceleration in the vertical direction $\Gamma = A_\mathrm{v}\left(2\pi f\right)^2/g$ is calculated to be 5.60. The horizontal oscillation amplitude in the center of the channel A_h was 1.87 mm. Accordingly every point of the channel floor followed approximately a circular trajectory in a plane tangent to the ring.
The amount of material in the container is given by the number of particle layers H_0 that form when the material is evenly distributed around the ring and the particles are close-packed. A densely packed monolayer consists of 21,500 particles. In the experiments H_0 was varied from 3 up to 19 in steps of 0.5.

4.3 Results

For $H_0 \leq 8.5$ or $H_0 \geq 15.5$ the uniform material distribution is stable. In both cases manually generated heaps and holes decay within seconds. Shallow beds ($H_0 \leq 8.5$) are flat and oscillate at the forcing frequency. Deep beds ($H_0 \geq 15.5$) exhibit subharmonic waves with constant envelope throughout the whole channel (Faraday 1831; Douady et al. 1989; Melo et al. 1994; Bizon et al. 1998; Sano 2005). Within the intermediate regime, $8.5 < H_0 < 15.5$, the uniform material distribution is unstable for $H_0 < 12.0$, decaying spontaneously into regions of decreased bed thickness that are flat and oscillate at the forcing frequency and regions of increased bed thickness where standing waves are present. After a coarsening process of about 1 min regions of increased bed thickness have merged into a single pulse of subharmonic waves (see Fig. 4.2). Bistability of the uniform material distribution and the pulse state is observed for $12.0 \leq H_0 < 15.5$. In this range either extended or localized waves are observed. To check whether the pulse is also present under pure vertical forcing the horizontal oscillation component was turned off by changing

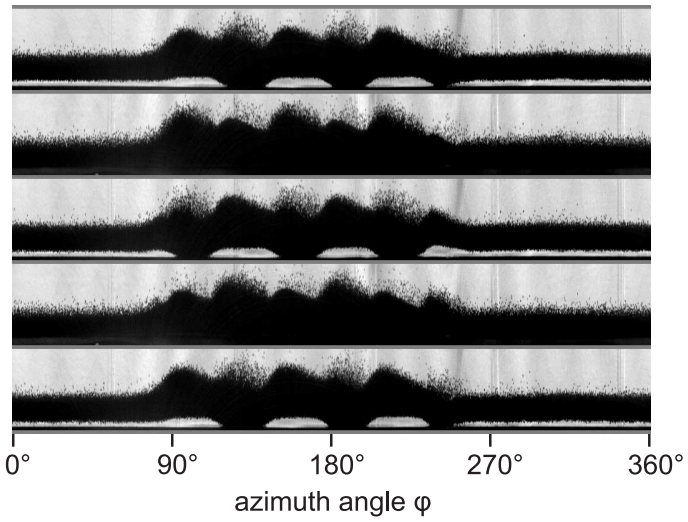

Figure 4.2: Panoramic snapshots through the inner sidewall of the channel. Time increases from top to bottom in steps of half a forcing period. For clarity the images are stretched vertically by a factor of 3.5. The total amount of material in the container corresponds to $H_0 = 12.0$ particle layers.

the machine settings. In consequence uneven material distributions became unstable and particle diffusion led to an equal bed thickness in the whole container. Hence the horizontal driving component is essential for a pulse to exist.

In order to elucidate the spatiotemporal dynamics of the bed undulations we plot the gap width between the container floor and the layer bottom in gray scale as a function of azimuth angle and time. The sideviews are divided into 1024 vertical stripes ranging from the bottom of the container to the middle of the bed (see Fig. 4.3). The mean brightness of each stripe is then taken as a measure of the local gap width.

Fig. 4.4 depicts the gap width for the situation of Fig. 4.2: Outside the pulse the gap width is constant in space and the layer detaches from the floor every forcing cycle. Within the pulse the layer is undulated and the oscillation frequency is half the forcing frequency. Both the wave pattern and the pulse drift to the left, yet at a different velocity, the pulse being about two times faster than the waves. This implies that new waves are constantly created at the leading front of the pulse whereas the last wave in the pulse is shrinking. As soon as the last wave falls below a critical size it detaches from the pulse, slows down, and even reverses its direction of movement until it dissolves completely.

To separate the slow dynamics of the pulse envelope from the rapid oscillations of the substructure one image per forcing cycle was recorded at a fixed phase. Since the period doubling is not of interest here we average two successive images. A measure for the bed extension, as depicted in Fig. 4.5b, was obtained by a technique similar to the one used

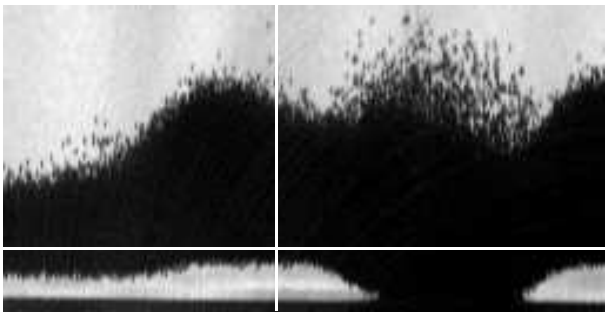

Figure 4.3: Fragment of the topmost image of Fig. 4.2. To obtain measures for the gap width and the bed extension as a function of the azimuth angle, gray values are averaged over vertical stripes. Their width is equal to the white vertical line. For the gap width calculation only the lower part of the image up to the white horizontal line is used.

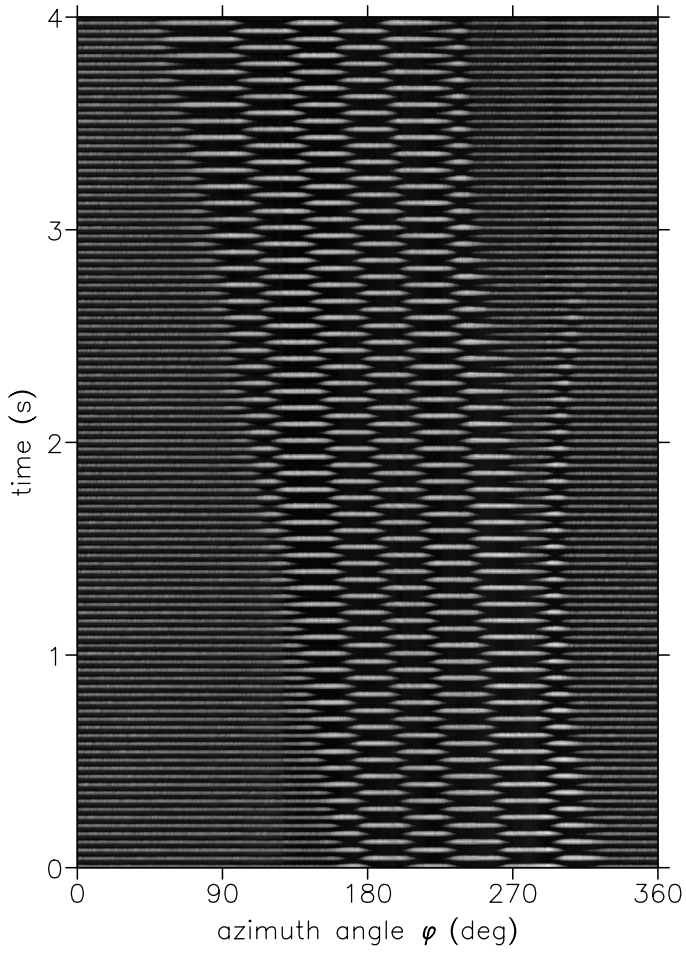

Figure 4.4: Width of the gap between the container floor and the layer bottom as a function of azimuth angle φ and time, coded in gray scale. The brightest regions correspond to a gap width of approximately $10\,d$.

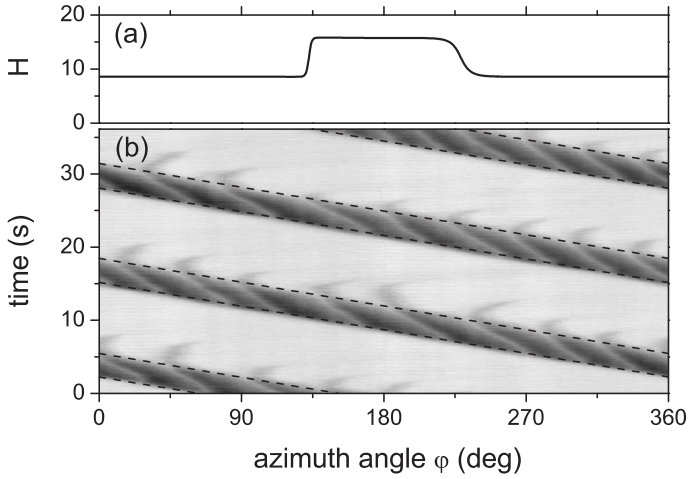

Figure 4.5: Travelling pulse observed at $H_0 = 10.5$. (a) Local bed height in the steady state as obtained from the model. (b) Measured vertical bed extension as a function of azimuth angle φ and time, coded in gray scale. The darker the thicker is the bed. Broken lines indicate linear fits to the front positions.

to extract the gap width. The major difference was that here we calculated the mean brightness of vertical stripes that cover the whole image instead of only the lower part (see Fig. 4.3). The space-time plot shows a pulse with constant length and velocity performing several revolutions in the annular container. Positions of leading and trailing fronts are determined by largest gradients. The pulse velocity is determined by fitting straight lines through the detected positions.

To shed light on the mechanism behind the phenomenon of localized pattern formation, we determined the transport velocity $v_t(H_0)$, defined for steady states with uniform material distribution as the particle velocity along the channel averaged over all particles and many forcing cycles. In fact we measured the time that a large ($d = 1\,\mathrm{cm}$) wooden tracer particle needed to travel a certain distance. By visual inspection we conclude that the mean tracer velocity is representative for the transport velocity. This is also corroborated by experiments in a linear channel by Grochowski et al. (2004) where the transport velocity, determined by simultaneous measurement of the mass flow and the total amount of material in the trough, was compared to the velocity of tracer particles.

The tracer particle is subject to Brownian motion with a diffusion constant of about $1\,\mathrm{cm}^2/\mathrm{s}$. This value was extracted from the deviations from the mean time the particle needs to perform one revolution in the annular channel. Total observation times exceeded 200 s in order to keep the error for the transport velocity below $0.1\,\mathrm{cm/s}$.

In region I of Fig. 4.6 the transport velocity is positive (in the direction of increasing angle φ) and grows linearly with H_0. The uniform material distribution is unstable in region II,

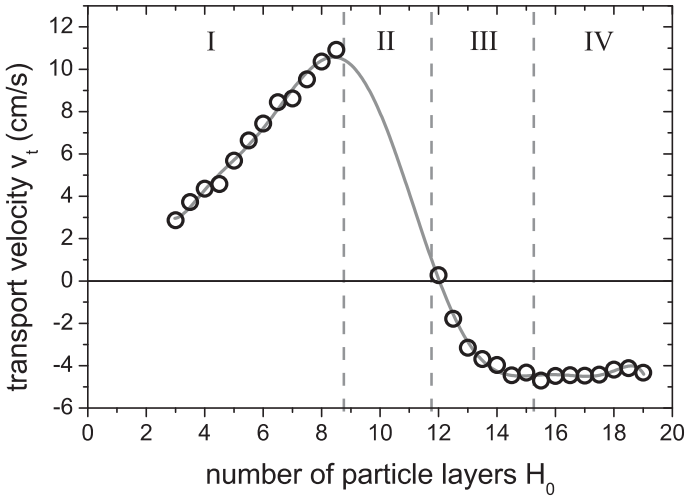

Figure 4.6: Transport velocity v_t of the granular material as a function of the number of particle layers H_0. The curve represents a 9th order polynomial fit used in the model.

preventing the determination of the transport velocity in this range. In regions III and IV the transport velocity decreases, becomes even negative, and finally attains a constant value. In the latter regions subharmonic waves are present that drift with the same velocity as the tracer particle. The different transport behavior below and above region II is due to the transition from periodic to period-doubling dynamics. Beds consisting of less than 8.5 particle layers are in contact with the container floor at different intervals of the driving period than beds with more than 12.0 particle layers. Thus the local bed thickness via the corresponding oscillation dynamics affects the local transport velocity (Grochowski et al. 2004; El hor and Linz 2005), which in turn leads to a change in local bed thickness.

4.4 Model

To conceive this mechanism, we adopted a one-dimensional continuum model for the granular flow. The measured bed-height dependent transport velocity was taken as input, while details of the granular dynamics were neglected. We introduce a local bed height $H(x,t)$, where x denotes the position along the ring and t the time, which satisfies $\int_0^L H(x,t)\,dx = H_0 L$. The continuity equation for this local bed thickness reads

$$\frac{\partial H}{\partial t} + \frac{\partial\,(Hv)}{\partial x} = 0 \quad , \tag{4.1}$$

where $v(x,t)$ is the local flow velocity. The analogue of the Navier-Stokes equation can be written as

$$\frac{\partial v}{\partial t} + v\frac{\partial v}{\partial x} = -\frac{1}{H}\frac{\partial p}{\partial x} + \frac{f_e}{H} + \frac{1}{H}\frac{\partial}{\partial x}\left(\mu\frac{\partial v}{\partial x}\right) \quad . \tag{4.2}$$

For p, the equivalent of the pressure, we took $p = c_0^2 \cdot H$ with constant c_0 in order to model the tendency of the particles to move against the local bed height gradient. The analogue of the force density is given by

$$f_e = H \cdot \frac{v_t(H) - v}{\tau} \quad .$$

This ansatz implies that for uniform material distributions the granulate attains the velocity $v_t(H)$ by an exponential relaxation process with a time constant τ. To avoid numerical artifacts connected with kinks we assume $v_t(H)$ to be a smooth function and approximate the experimental transport velocity data by a polynomial (see Fig. 4.6). The analogue of the viscosity μ is assumed to be constant. Eq. (4.2) then becomes

$$\frac{\partial v}{\partial t} + v\frac{\partial v}{\partial x} = -\frac{c_0^2}{H}\frac{\partial H}{\partial x} + \frac{v_t(H) - v}{\tau} + \frac{\mu}{H}\frac{\partial^2 v}{\partial x^2} \quad . \tag{4.3}$$

Depending on the parameters, the steady-state solution of model (4.1) and (4.3) is either a homogeneous flow or a traveling pulse of fixed shape (Fig. 4.5a). Linearizing Eqs. (4.1) and (4.3) around $H = H_0$ one finds that the homogeneous flow is stable against a perturbation with the wave vector $q = 0$ if

$$H_0 \cdot \left| \frac{\partial}{\partial x} v_t(H_0) \right| < c_0 \quad . \tag{4.4}$$

Since it has been shown by Kerner and Konhäuser (1993) and Kurtze and Hong (1995) that the instability first occurs for $q = 0$, if condition (4.4) is fulfilled, the flow is stable against any perturbation.

Guided by experimental observation we chose $\tau = 0.1\,\mathrm{s}$, corresponding to about three forcing cycles. Note that τ is small compared to the time it takes for the material to travel through the pulse. In this limit, the pressure and diffusion terms in Eq. (4.3) can be neglected everywhere except at the fronts, and the pulses exhibit a plateau where $v = v_t(H)$ (Fig. 4.5a). We verified that in this limit the results are insensitive to τ. The viscous term was kept just large enough to stabilize the leading front and sufficiently small not to influence significantly the results. A value $\mu = 50\,\mathrm{cm}^2/\mathrm{s}$ has been chosen, resulting in a rather steep leading front which corresponds to the experimental observation (see Fig. 4.2). The only vital parameter of the model is thus c_0.

4.5 Comparison between simulation and experiment

Increasing H_0 enlarges the pulse (see Fig. 4.7b). The region of stability for the pulse solution obtained from the model matches the experiments best when choosing $c_0^2 = 600\,\mathrm{cm}^2/\mathrm{s}^2$. Then the model gives stable homogeneous flow for $H_0 < 9.66$ or $H_0 > 13.18$,

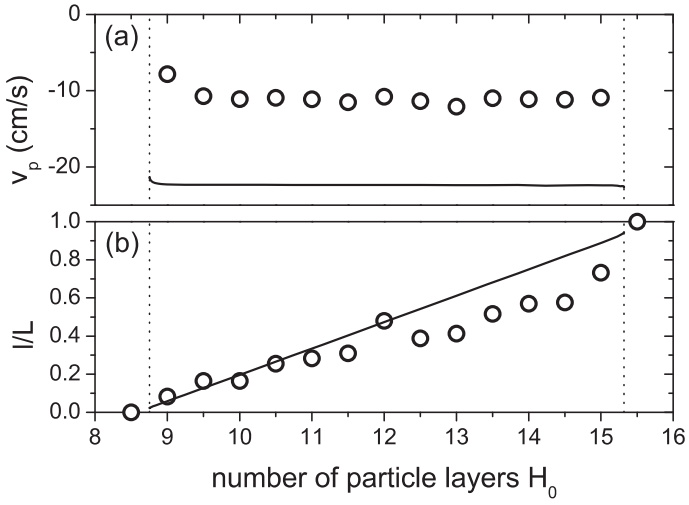

Figure 4.7: (a) Measured pulse velocity v_p and (b) relative pulse length l/L as functions of the number of particle layers H_0, and comparison with the model (solid lines). Dotted lines demarcate the region of stability for pulses.

and a stable pulse for $8.75 < H_0 < 15.32$. In case the homogeneous flow is unstable, several pulses, generated by small perturbations, coalesce to a single steady pulse on the time scale of a minute, in agreement with experiment. According to the model the pulse solution bifurcates subcritically at $H_0 = 9.66$ and $H_0 = 13.18$, respectively. Hence there exist two bistable regions. Given that only one parameter was adjusted, the match in pulse length between theory and experiment in the whole range of H_0 is remarkable. The pulse velocity v_p, displayed in Fig. 4.7a, is almost constant amounting to about $-11\,\mathrm{cm/s}$ except for the shortest pulse which is approximately 30 % slower. The model also gives an almost constant pulse velocity. Why it is a factor of two off remains an open question. Strikingly the chosen value of $c_0 = 24\,\mathrm{cm/s}$ is of the same order of magnitude as the container speed, which amounts to $32.6 \pm 1.1\,\mathrm{cm/s}$ and can be taken as the typical speed transmitted to a particle upon collision with the container floor. The prefactor of the last term in Eq. 4.3 can be considered as velocity diffusion constant. For beds consisting of more than ten particle layers it is comparable in magnitude to the tracer particle's diffusion constant. Another interesting aspect of the model is the fact that the bed height inside and outside the pulse always differ by $|H_2 - H_1| = 7.2$ independent of H_0. Only the length of the pulse grows when material is added.

4.6 Conclusion

In conclusion, around the transition to period doubling dynamics drastic changes in the transport velocity produce localized subharmonic wave packets in a circularly vibrated

bed. Standing waves appear throughout a pulse of increased bed thickness. The pulse arises from a subcritical bifurcation and obtains a plateau-like shape. Its length increases when material is added while its velocity remains constant. As in earlier experiments on the sublimation of a vibrated monolayer (see Chapter 5) two regions with different particle coverage coexist. However in that case phase separation was still observed for pure vertical forcing when no material transport occurs.

Waves that appear if the local velocity in a one-dimensional, compressible flow is a function of the local density are called kinematic waves (Whitham 1974). One example are density waves in granular flows in a vertical pipe described by Moriyama et al. (1998), where the sedimentation rate is a nonlinear function of the local particle density. In the context of road traffic the fundamental diagram describes the connection between flow rate and vehicle density (Nagatani 2002; Helbing 2001). Equations (4.1) and (4.3) are inspired by a traffic flow model used by Kerner and Konhäuser (1993) and Kurtze and Hong (1995) that explains the spontaneous appearance of pulses — "phantom jams" — out of initially homogeneous flow. Plugging in the measured transport velocity as function of bed thickness our model for the dynamics of the material distribution retains the basic features of the pulses seen in the experiments.

Chapter 5

Sublimation of a vibrated monolayer

The fluidization of a monolayer of glass beads in a horizontally and vertically vibrated annular container was studied. At peak forcing accelerations between 1.1 g and 1.5 g a solid-like and a gas-like domain coexist. The solid fraction decreases with increasing acceleration and shows hysteresis. The sharp boundaries between the two regions travel around the channel faster than the particles are transported. Complementary to the experimental studies a molecular dynamics simulation was used to extract local granular temperature and number density. It was found that the number density in the solid phase is several times that in the gas, while the temperature is orders of magnitude lower.
The event-driven molecular dynamics simulations were conducted by Jennifer Kreft from the Center for Nonlinear Dynamics at the University of Texas, who spent three months in Bayreuth as a visiting scientist working on this project.
The results of this collaboration have been published as a Physical Review Letter (Götzendorfer et al. 2005).

5.1 Introduction

Dry ice (solid CO_2) at atmospheric pressure provides an example of the phenomenon called sublimation i.e. the direct transition of a substance from the solid to the gaseous state. In nature this phenomenon is observed in the dry valleys at the margins of Antarctica (Hawes et al. 2003), and technologically exploited for the production of instant coffee by freeze-drying. In this chapter a quantitative characterization of sublimation occurring as a nonequilibrium phase transition in a granular system is presented.
Granular material, i.e. an ensemble of macroscopic cohesionless particles, undergoes phase transitions between solid-like, liquid-like, and gas-like states (Jaeger et al. 1996). Since collisions between grains are inelastic, energy must be constantly fed into the system in order to maintain a fluid phase, i.e. a granular liquid or gas is always away from

equilibrium.

Coexistence of different phases is known to accompany the fluidization of granular material. For example, submitting a two-dimensional vertical packing of beads to vertical or horizontal vibrations fluidizes the upper layers, while the lower lying material still maintains a crystalline structure (Clément and Rajchenbach 1991; Gallas et al. 1992; Ristow et al. 1997). Likewise, investigations into the fluidization of a vertically vibrated horizontal submonolayer by Olafsen and Urbach (1998), Losert et al. (1999), Nie et al. (2000), and Prevost et al. (2004) demonstrated that domains of different phases can coexist. In a recent experiment with the same geometry Reis et al. (2006) discovered a regime intermediate between isotropic fluid and crystalline. But the system size was too small for the authors to decide whether they dealt with a coexistence region or a homogenous hexatic phase with long range orientational order but no positional ordering. Coarse graining of the coexisting phases has been quantitatively characterized in electrostatically driven granular material by Aranson et al. (2000) and Sapozhnikov et al. (2003). Other examples for driven systems where the equipartition of kinetic energy is violated are bidisperse mixtures (Wildman and Parker 2002; Feitosa and Menon 2002; Barrat and Trizac 2002) and monodisperse systems in a container separated into two compartments by a wall (Schlichting and Nordmeier 1996; van der Weele et al. 2001). The latter experiment became popular as the granular 'Maxwell's demon'(Eggers 1999).

This chapter deals with a monodisperse system where equipartition of energy is violated by coexisting gaseous and solid domains, even though particle motion is fully three-dimensional and not restricted by guiding partitions. The solid phase revolved in an annular channel demonstrating that the coexistence of solid and fluid regions is not caused by small potential inhomogeneities in the forcing, particle container interactions or a tilt of the apparatus.

5.2 Experiment

With the mounted unbalanced masses the amplitude in the vertical direction, A_v, decreased slowly with frequency from 2.27 mm to 2.22 mm. The horizontal amplitude, A_h, in the center of the channel was $93.4 \pm 0.5\%$ of the vertical amplitude. Accordingly every point of the channel floor followed an almost circular trajectory in a plane tangent to the ring. For the experiments a densely packed monolayer of spherical basalt glass beads (density $\rho = 3.0\,\mathrm{g/cm^3}$) with diameter $d = 1.18 \pm 0.03\,\mathrm{mm}$ was prepared on the channel floor. Its mass corresponded to 21,500 particles. The granular system was observed from the top via a conical mirror placed in the center of the ring. One image per forcing cycle was recorded at a fixed phase using an electro-optical triggering system.

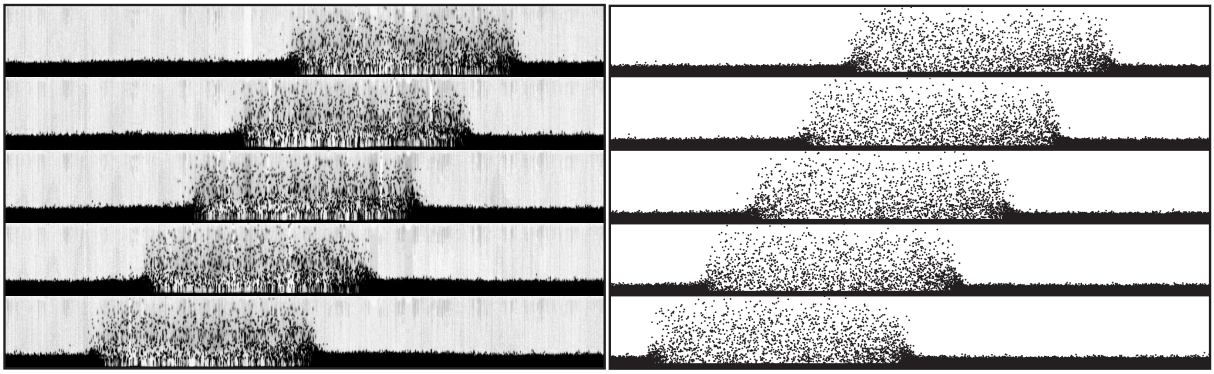

Figure 5.1: Snapshots through the inner side wall of the channel covering 360° from experiment (left) and simulation (right) taken at $z(t) = 0$ during the downward motion of the container. Here the system sizes of simulation and experiment are equal. Time increases from top to bottom by 1.72 seconds (20 cycles) between consecutive snapshots. For clarity all images are stretched in the vertical direction by a factor of four. ($f = 11.6\,\mathrm{Hz}$, $\Gamma = 1.23$)

5.3 Simulation

To have access to the positions and velocities of all particles, experiments were replicated using a three-dimensional molecular dynamics simulation applying an event-driven algorithm described by Bizon et al. (1998). When not mentioned explicitly the length of the system L_0 and the number of particles was one quarter of those in the experiment to decrease the calculation time. The entire channel moved both vertically and horizontally with the same values of f, A_v, and A_h as in the experiment. The parameters characterizing changes in relative surface velocity for both ball-ball and ball-wall collisions were the coefficient of sliding friction $\mu = 0.5$ and the maximum rotational coefficient of restitution $\beta_0 = 0.35$. These values were chosen because they successfully reproduced surface wave patterns observed in vertically vibrated granular media (Bizon et al. 1998). To match the minimum layer depth required for surface wave formation in experiment the coefficient of normal restitution for interactions between particles, e, was set to 0.97. The coefficient of restitution with the walls was the only fit parameter and a value of 0.93 was found to quantitatively reproduce the experimental results. To prevent inelastic collapse the coefficient of normal restitution for both types of collisions approaches unity as the normal velocity v_n approaches zero according to $\max(e, 1-(1-e)(v_\mathrm{n}/\sqrt{gd})^{3/4})$.

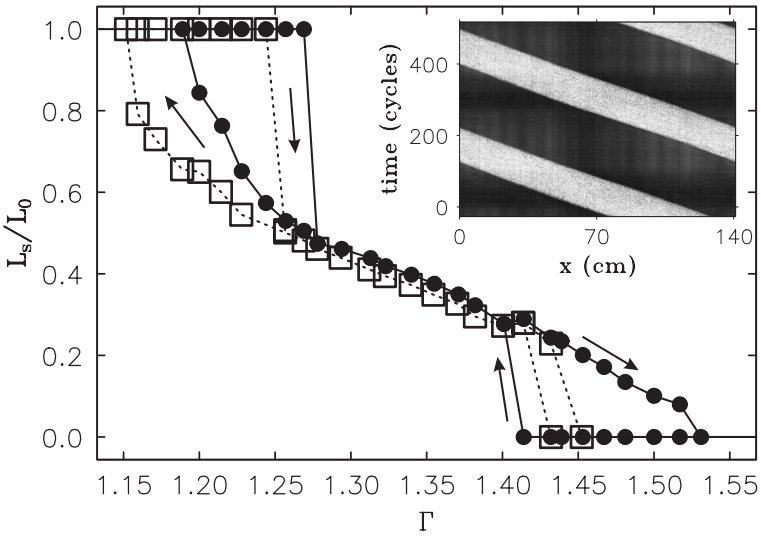

Figure 5.2: Solid fraction L_s/L_0 as a function of the peak container acceleration Γ in experiment (filled circles) and simulation (open squares). Arrows indicate how the system evolves in the hysteresis loops. The inset is a space-time diagram of Δn (see text for definition) from experiment for the parameters of Fig. 5.1. Solid regions appear dark.

5.4 Results

If the granulate is driven at peak dimensionless accelerations $\Gamma = (2\pi f)^2 A_\mathrm{v}/g$ up to 1.1 the grains spread homogeneously in the channel. In close-up high-speed movies the whole monolayer looks like a single completely inelastic object. The particles basically maintain their relative positions. Above $\Gamma = 1.5$ the granular material is fully fluidized and resembles a gas (Pöschel and Luding 2001). Particles jump some centimeters (several tens of particle diameters) high, and their motion seems to be random. At intermediate forcing ($1.20 < \Gamma < 1.52$) both phases can coexist as demonstrated in Fig. 5.1. Starting from a homogeneous, solid monolayer fluidized regions first appear at $\Gamma = 1.28$. In contrast, arriving from a completely fluidized state density fluctuations lead to gas collapse and the formation of solid regions at $\Gamma = 1.40$. At Γ values between the spontaneous creation of one of the two phases and the limits of the coexistence region, the system is hysteretic. The generation of coexisting phases usually gives rise to several separated solid and fluid domains. Condensed regions merge to form a single solid domain surrounded by gaseous granulate after approximately 10 minutes. Thenceforward this single solid domain stays intact, preserving its dimensions. The phase boundary is remarkably sharp and always small compared to the size of the solid and gas phases. The boundaries between the solid and fluid regions travel along the channel due to the presence of a horizontal oscillation component inducing material transport (Grochowski et al. 2004; Rouijaa et al. 2005).

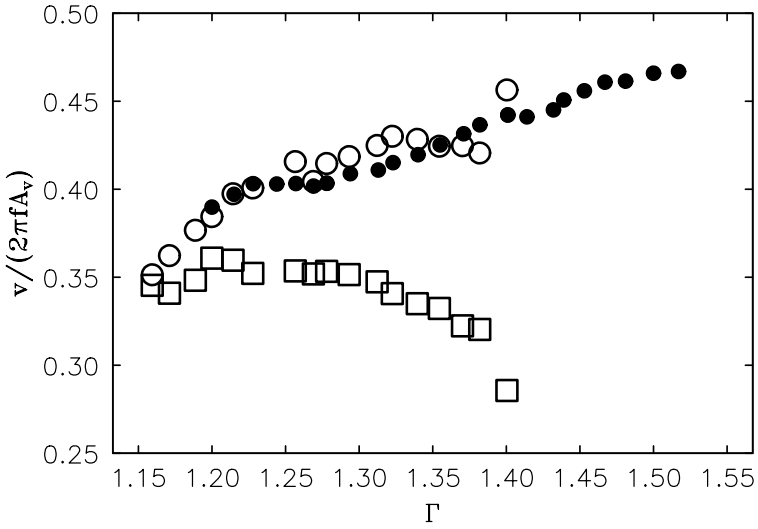

Figure 5.3: Dimensionless velocity $v/\left(2\pi f A_v\right)$ of the phase boundaries as a function of the peak container acceleration Γ in experiment (filled circles) and simulation (open circles). Open squares indicate the mean transport velocity obtained from numerical simulations.

For the determination of the solid fraction, i.e. the length of the solid region divided by the circumference of the channel, L_s/L_0, and the velocity of the phase boundaries side views as shown in Fig. 5.1 are used. The density difference Δn between a lower and an upper region in the container serves as an order parameter for the two states. The lower region ranges from the container floor to the surface of the solid phase (obtained from the maximum density gradient), while the top region extends from there to a height of $30\,d$ (corresponding to the height shown in Fig. 5.1). A measure for the density is determined from the average gray value in experiment or the number density in simulation. In the solid phase Δn will be high while in the gas phase a low value will result. This order parameter, coded in gray scale, is plotted as a function of horizontal position x and time in the inset of Fig. 5.2. The phase boundaries are determined from the largest gradients in these plots after short wavelength fluctuations have been filtered out. The lengths of the condensed phase and the velocities of the phase boundaries are constant once the coarsening process is over.

The length of the solid phase L_s shown in Fig. 5.2 declines sharply from complete coverage to about half the circumference within the lower hysteretic region. It follows a more gentle virtually linear decrease for the rest of the range of coexistence. Simulation and experiment agree very well in the nonhysteretic part. In this region simulation results for the relative length of the condensed phase do not change when the system is four times longer. The deviations in the hysteretic regions, however, are partly a consequence of the shorter channel length in the simulations.

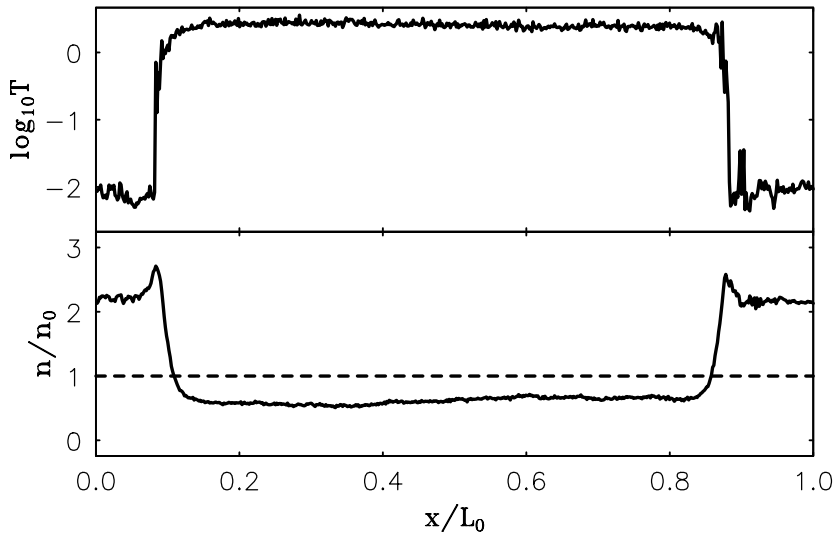

Figure 5.4: Dimensionless temperature (top) and number density (bottom) from simulations with purely vertical forcing and $\Gamma = 1.40, f = 12.53\,\mathrm{Hz}$. The broken line in the lower graph indicates the average number density.

In Fig. 5.3 the dimensionless velocity $v/(2\pi f A_v)$ of the phase boundary is given as a function of Γ. It exhibits an approximately linear increase in the range of coexistence. Additionally the mean transport velocity was calculated from the particle displacements in the simulation over 50 forcing cycles. Its decline with increasing Γ is a consequence of the particles in the gas phase being transported less efficiently than those in the solid phase, as observed in experiment. The difference in transport velocity for the two phases also implies a continuous deposition at the front of the condensed phase and sublimation at the end. This cyclic process of solidification and fluidization causes the gap between the mean transport velocity and that of the phase boundary.

For the numerical investigation of the granular temperature and number density the simulations were started from the circularly forced case after all transients have died out. It turned out that the coexistence remains stable after switching off the horizontal forcing. The channel was subdivided into thin vertical slices and the number of particles in each of them counted and normalized by the average value n_0. In order to obtain a measure for random velocity fluctuations, the normalized granular temperature T was defined as the mean square horizontal velocity per slice divided by the gravitational acceleration and the particle diameter, $\langle v_{\mathrm{hor}}^2 \rangle / gd$. The horizontal velocity component was chosen because, at any phase of the driving, the mean horizontal velocity vanishes. In addition there is no direct dependence of a particles' horizontal velocity on its position in the field of gravity. This is not the case for the vertical velocity component, which makes it much more difficult to extract random velocity fluctuations in the vertical direction. Fig. 5.4

Figure 5.5: Sketch of the particle fluxes across the phase boundary for pure vertical forcing. The background image is taken from Fig. 5.1b.

contains a showcase result featuring a gas phase with a granular temperature two orders of magnitude higher than in the solid, while its number density is a factor of 3.5 lower.

5.5 Conclusion

In conclusion this system allows a quantitative characterization of sublimation and the coexistence of gas and solid phases in granular matter. This is due to the additional horizontal oscillation component which makes the pattern rotate, and thereby demonstrates that the coexistence of solid and fluid regions is not caused by small potential inhomogeneities in the forcing, particle container interactions or a tilt of the apparatus. The horizontal forcing also assists the coarsening process because the transport velocity in the solid regions increases slightly with their length. Larger solid regions catch up to smaller ones and incorporate them until all solid regions have merged. This process is irreversible. Finally a unique time independent state with constant length of the solid phase and constant velocities of the phase boundaries is established.
The simulations show that the number density in the solid phase is several times that in the gas, while the granular temperature is two orders of magnitude lower. That ratio is less extreme for the vertical component of the kinetic energy, namely only about a factor of two. Such a lack of equipartition of energy is allowed in nonequilibrium systems.
An open question remains why and how a constant solid fraction is established. Part of the answer can be extracted from numerical simulations as presented in Fig. 5.5. The particles in the solid region which are close to the phase boundary will diffuse towards the more dilute gas phase. When they cross the phase boundary they fluidize. In the steady state this flux is balanced by solidifying gas particles, which enter the solid region through ballistic jumps. If the solid phase shrinks due to fluctuations the gas density increases because the solid phase possesses a higher number density. This leads to an increase in the back flux of particles from the gas towards the solid, while the diffusion from the solid to the gas phase remains constant. Therefore the solid state expands again thus stabilizing the steady state solid fraction.
While in equilibrium phase transitions minimization of free energy determines the rela-

tive amounts of gas and solid phases in contact with a common heat bath, there is no recognized free energy for granular materials as pointed out by Prevost et al. (2004). Future detailed studies of this system might offer insight into what plays the role of free energy here. The nature of the coexistence of gas and solid in shaken granular matter with a self-stabilizing discontinuous jump of density and temperature across the boundary remains an intriguing phenomenon.

Chapter 6

Setup for vertically agitated 2D packings

To investigate the transition of a crystalline particle packing to a fully fluidized state a separate setup was used. Particles were confined to two dimensions in order to keep them visible at all times. With the help of a high speed camera all particles could then be traced. The vibration was restricted to the vertical direction. The experiment was designed flexible enough to allow an easy variation of driving parameters and the use of particles of various sizes.

The driving vertical sinusoidal oscillation is generated by an electromechanical vibration exciter (Brüel & Kjær 4808). For experimental runs the frequency was adjusted to 20, 30, 40, 50 or 60 Hz with an accuracy of 0.1 %. The maximum container acceleration was monitored via an oscilloscope receiving its input signal from an accelerometer mounted on the vibration exciter below the particle container (see Fig. 6.1). In each run the maximum container acceleration was gradually raised starting from a value of 1.0 g, when the particles do not yet leave the ground up to a value of 9.0 g in steps of 0.2 g, where g is the earth's gravitational acceleration.

The granular packing consisted of spherical, monodisperse particles confined between two vertical glass plates, the separation of which was only 0.2 mm larger than the particle diameter. At this gap width effects of friction between the particles and the back and front container walls were small (van Zon et al. 2004). Particles with diameters d of 4, 6, 8, and 10 mm were used. In order to have well defined starting conditions they were initially arranged to form a perfect single crystal . Therefore we chose the width of the container such that an integer number ofparticles just fit in the bottom layer, namely a width of 198 mm for the particles with $d = 6$ mm and 200 mm for the other particle sizes. The container floor and sidewalls were made of polyvinyl chloride (PVC).

The system was lighted through diffusive parchment paper attached to the outer side of the

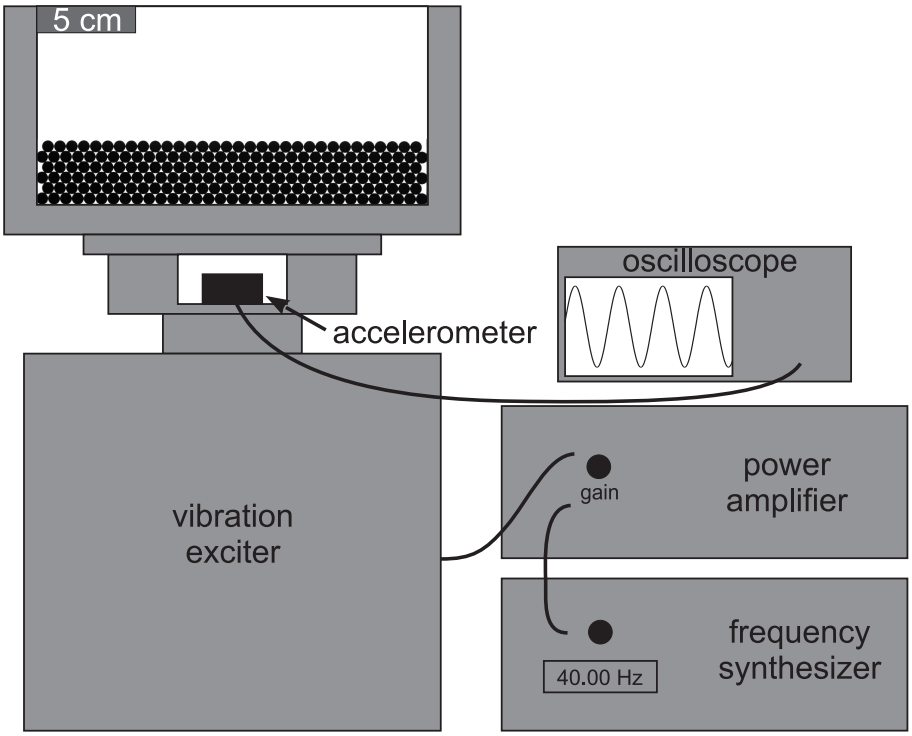

Figure 6.1: Setup for the vertical shaking experiments.

rear glass plate. Thus the particles appear black in front of a bright background. Images were recorded with a digital high speed camera (Redlake Motion Pro 500) at a rate of 500 images per second with an exposure time of 1 ms and a resolution of 1024×500 pixel. As long as the bed remained in its perfect crystalline state good averages of particle density and displacements could be obtained from the analysis of 400 images. For higher forcing this number was doubled to 800 images.

The particle positions were extracted from the recorded images using a correlation method. A brightness pattern resembling the one of a single particle was correlated with the image. The highest local maxima of the correlation function then indicate the particle positions. The threshold value was chosen such that in each image all particles were found. Subpixel resolution was achieved by a parabolic interpolation around the local maxima.

Most experiments were done with glass beads, but also steel, polyamide and aluminum spheres were under investigation. Their elasticity can be characterized by the coefficient of restitution, which is the ratio of the velocities after and before a collision in the center of mass frame. We measured the coefficient of restitution for collisions between the particles and plates made of PVC and glass, i.e. the container materials, as well as for particle-particle collisions. The results are summarized in Table 6.1. To determine e_{PVC} and e_{glass} the sound produced by a particle bouncing on the PVC or glass plate was recorded and analyzed (Bernstein 1977; Smith et al. 1981; Stensgaard and Lægsgaard 2001). From

material	ρ (g/cm^3)	e_{PVC}	e_{glass}	e_{pp}
glass	2.5	0.93	0.98	0.90
steel	7.7	0.93	0.98	0.88
polyamide	1.5	0.96	0.97	0.62
aluminum	2.7	0.88	0.49	0.1

Table 6.1: Density ρ of the utilized particles, and their coefficient of restitution for collisions with a PVC plate e_{PVC}, a glass plate e_{glass} and particles of the same material e_{pp}.

the time intervals between successive impacts the coefficient of restitution was calculated. We observed that e_{PVC} and e_{glass} slightly depend on the impact velocity. To allow a comparison of the elasticity of different collisions the values in Table 6.1 all refer to an impact velocity of 1 m/s. The effect of the particle size on the value of the coefficient of restitution was found to be negligible, at least in the range of particle sizes used for the experiments. The particle-particle coefficient of restitution e_{pp} was determined by a collision experiment in which a spherical particle rolled down a slope over a jump. After leaving the jump, at the apex of its ballistic trajectory, 22.5 cm above the ground, the particle horizontally hit another particle at rest. Knowing the impact velocity, the measurement of the distance between the collision point and the point where the particles touched the ground yields e_{pp}.

Chapter 7

Granular meltdown

In this chapter measurements of the fluidization process in vertically vibrated two-dimensional granular packings are presented. An initially close packed granular bed was exposed to sinusoidal container oscillations with gradually increasing amplitude. At first the particles close to the free surface become mobile. When a critical value of the forcing strength is reached the remaining crystal suddenly breaks up and the bed fluidizes completely. This transition leads to discontinuous changes in the density distribution and in the root mean square displacement of the individual particles. Likewise the vertical center of mass coordinate increases by leaps and bounds at the transition. It turns out that the maximum container velocity v_0 is the crucial driving parameter determining the state of a fully fluidized system. For particles of various sizes the transition to full fluidization occurs at the same value of v_0^2/gd, where d is the particle diameter and g is the gravitational acceleration. A discontinuous fluidization transition is only observed when the particles are highly elastic.
The content of this chapter has appeared as a regular article in Physical Review E (Götzendorfer et al. 2006).

7.1 Introduction

The behavior of vibrated granular matter is of paramount importance to many industrial processes and is therefore studied extensively by engineers (see for example Alexeev et al. (1999), Thomas et al. (2000), or Tai and Hsiau (2004)). But also within the physics community the fluidization of granular beds by vibration has evolved into a very active field of research during the last fifteen years. Back in 1990 Evesque et al. demonstrated that the surface of a sand pile is capable of flowing, if a sufficiently strong vertical vibration is applied to the pile. The thickness of the fluidized surface region increases steadily with increasing vibration frequency, yet the internal part of the heap remains compacted.

Surface fluidization was also reported from experiments by Clément and Rajchenbach (1991) on two- dimensional vertical packings of spheres and molecular dynamics simulations of the same system by Gallas et al. (1992). Furthermore the simulation could show that it is not — as previously suspected — the peak container acceleration that characterizes the onset of full fluidization, i. e. the transition to a state where all particles perform random walks and explore the whole container. Other simulations of two-dimensional systems by Luding et al. (1994) focus on the scaling behavior of the center of mass height in the fluidized regime. The authors point out that their simulation methods work well when the free flight time of the particles in between collisions is much longer than the collision time, but encounter problems when this is not the case. Thus reliable results could only be obtained well above the fluidization transition.

A theory for the liquid-solid transition of two-dimensional elastic hard spheres in the presence of gravity was devised by Quinn and Hong (2000). According to their model the granular bed fluidizes from top to bottom, the fraction of particles in the condensed regime decreasing linearly with the average kinetic particle energy which is assumed to be the same for all particles. They validated their prediction using an event-driven molecular-dynamics simulation, in which the completely elastic particles are in contact with a thermal heat reservoir that controls their average kinetic energy. It remains questionable whether this theory can be applied to assemblies of inelastic particles driven by an oscillating bottom plate. Especially since it has been reported recently by (Eshuis et al. 2005) that in deep, vigorously shaken beds a fluidized region forms at the bottom supporting a crystalline cluster hovering on top.

For the analysis of highly fluidized states in two dimensions velocity and density distributions were extracted from experiments and molecular dynamics simulations (Warr et al. 1995; Warr and Hansen 1996; Helal et al. 1997; Huntley 1998; Wildman et al. 1999; Wildman and Huntley 2000). Strong similarities were discovered between fluidized granular beds and molecular fluids in thermal equilibrium. Therefore kinetic theory could be applied to derive scaling laws for some experimentally accessible quantities.

Using positron emission particle tracking and nuclear magnetic resonance techniques, the motion of particles in three-dimensional fluidized beds was uncovered recently by Wildman et al. (2000) and Yang et al. (2002). The results turned out to be qualitatively very similar to those obtained in two dimensions.

Falcon et al. (1999) had a look at the collapse of three-dimensional beds that occurred at constant driving parameters, when the number of particles was increased. They reported a solidification transition from a regime where particles have erratic motions to a collective behavior where all the particles bounce like a nearly solid body. Later Mujica and Melo (2000) claimed that a solid-liquid-type transition occurs only at forcing frequencies below

the crossover frequency f_d given by $f_d = \sqrt{g/ld}$, where g is the gravitational acceleration, l the number of particle layers, and d the particle diameter.

This chapter focuses on the fluidization transition of an initially perfectly crystalline granular packing when the external forcing is increased. The influence of the vibration parameters, the particle size, and the material is studied.

These experiments pertain to the question about the nature of the melting transition in two dimensions. For equilibrium systems Kosterlitz, Thouless, Halperin, Nelson, and Young devised a theory, commonly referred to as KTHNY theory, that predicts a continuous two stage melting process (for a review see Strandburg (1988)). Since then the scenario predicted by the theory has been confirmed by experiments on various systems in thermal equilibrium. Most of these studies concerned colloidal systems involving screened Coulomb (Murray and VanWinkle 1987; Tang et al. 1989), electric dipole (Kusner et al. 1994), and magnetic dipole (Zahn et al. 1999; Eisenmann et al. 2004) interaction, but also a granular system of like-charged metal spheres (Tata et al. 2000) is among them.

Quinn and Goree (2001) found indications for a two-stage continuous melting transition in a non-equilibrium complex plasma consisting of microspheres suspended in a glow-discharge plasma. Olafsen and Urbach (2005) have shown that a horizontal monolayer of spheres confined between two vibrating plates exhibits a continuous transition from a hexagonally ordered solid phase to a disordered liquid that is well described by the KTHNY theory, too. Reis et al. (2006) experimented with a system of identical geometry where they replaced the smooth base plate by a roughened one. Their results are again consistent with a two-step continuous phase transition. The same behavior is observed in computer simulations during the crystallization transition of equilibrium hard disk systems in two dimensions conducted by Jaster (1999), Sengupta et al. (2000), and Watanabe et al. (2004). In contrast, if in the afore mentioned experiment the top plate is removed Olafsen and Urbach (1998) and Losert et al. (1999) have demonstated that the fluidization transition is discontinuous and hysteretic (see also Chapter 5). The goal of this work is to shed light on the nature of the fluidization transition of a vibrated two-dimensional vertical packing of spheres.

The experimental setup and procedure has already been described in Chapter 6. The remainder of this chapter is organized as follows: The experimental results together with their discussion are presented in Section 7.2. In Part 7.2.1 the fluidization transition is characterized by means of density distributions and root mean square particle displacements. Part 7.2.2 focuses on the center of mass height as an indicator of the state of fluidization. The influence of vibration parameters, particle properties, and bed thickness on the transition are studied. Finally Section 7.3 concludes by putting the presented work in the broader context of melting transitions in two-dimensional systems.

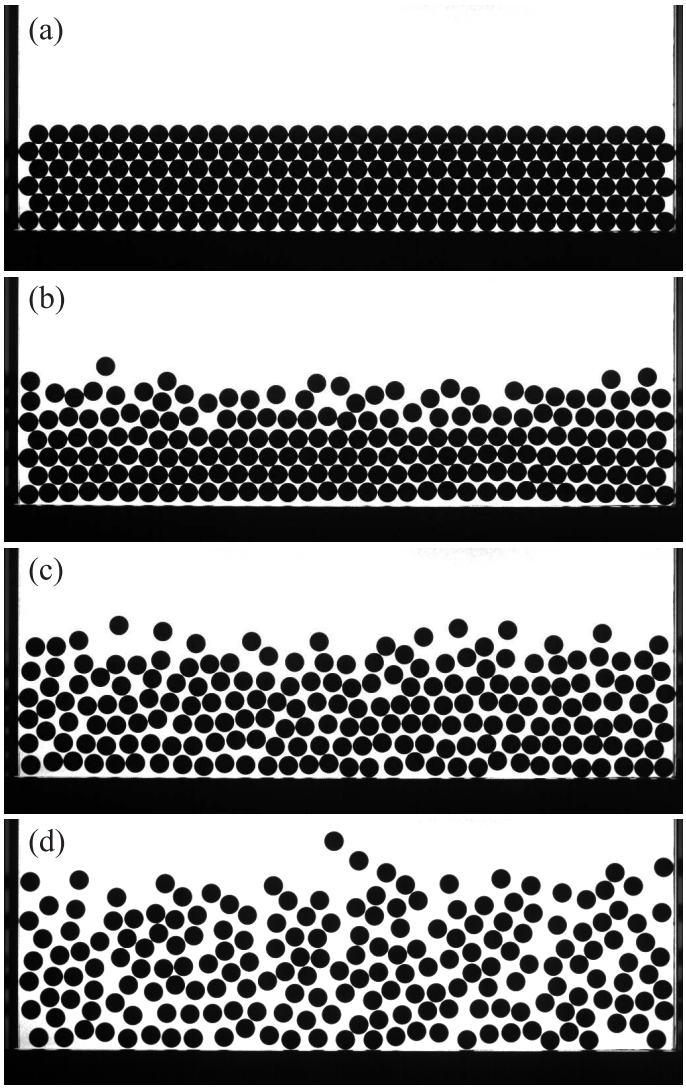

Figure 7.1: Snapshots of the granular bed at normalized peak container accelerations of (a) $\Gamma = 1.0$, (b) $\Gamma = 4.8$, (c) $\Gamma = 5.0$, and (d) $\Gamma = 7.4$.

7.2 Results and Discussion

7.2.1 The fluidization transition

Fig. 7.1 shows snapshots of a system of 195 glass particles, 6 mm in diameter, vibrated at a frequency $f = 40\,\mathrm{Hz}$, which were taken when the container was at its lowest position. The vibration amplitude A and the maximum container acceleration normalized by the acceleration of gravity Γ increase from top to bottom. For a sinusoidal oscillation these quantities are connected via $\Gamma = A\left(2\pi f\right)^2/g$. At $\Gamma = 1$ the particles stay in contact with each other and the container floor throughout the whole forcing cycle. Before starting the experiment the particles were arranged in perfect crystalline order as shown in Fig. 7.1a.

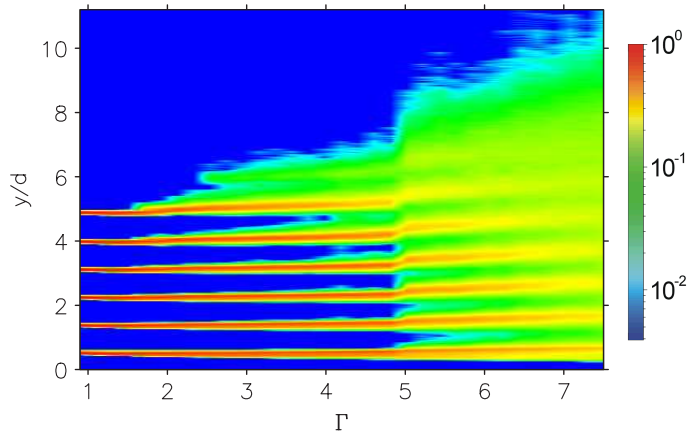

Figure 7.2: Logarithmically color coded histogram of the particle center positions, as function of height and the maximum container acceleration Γ. The histogram is normalized by its maximum value.

For higher values of Γ the bed as a whole clears the container floor performing ballistic jumps. The subsequent collisions of the particle assembly with the container floor are completely inelastic. With increasing Γ particles from the sixth layer start to move vertically with respect to their neighbors and at some point jump over them and form an additional layer. Then also the fifth layer starts to release particles, while the rest of the bed still preserves its crystalline order (see Fig. 7.1b). At a critical value of Γ the four bottom layers suddenly lose particles and fluidize. Fig. 7.1c shows the system just above this transition. Further raising Γ leads to an overall decrease in particle density (see Fig. 7.1d).
From the extracted particle positions the particle density ρ as a function of height y is calculated,

$$\rho\left(y\right) = \frac{1}{MN}\sum_{i}^{M}\sum_{j}^{N}\delta\left(y - y_{ij}\right) \quad ,$$

where y_{ij} is the vertical position of the jth particle in the ith image and i and j run over the number of analyzed images M and the number of particles in the system N, respectively. Fig. 7.2 shows the logarithmically color coded particle distribution histograms, obtained by integrating the density distributions over bins of 1/30 of a particle diameter d, for the examined range of Γ. The height coordinate y is normalized by d and its origin is fixed at the equilibrium container position. From $\Gamma \approx 1.8$ on the top layer widens towards the free surface until at $\Gamma = 2.6$ particles start to pop up. A transition in the whole bed takes place between $\Gamma = 4.8$ and $\Gamma = 5.0$. All peaks of the particle distribution histogram leap to larger heights and also their widths suddenly increase. The widening of the single layers adds up to a considerable expansion of the whole bed. With increasing Γ the bed

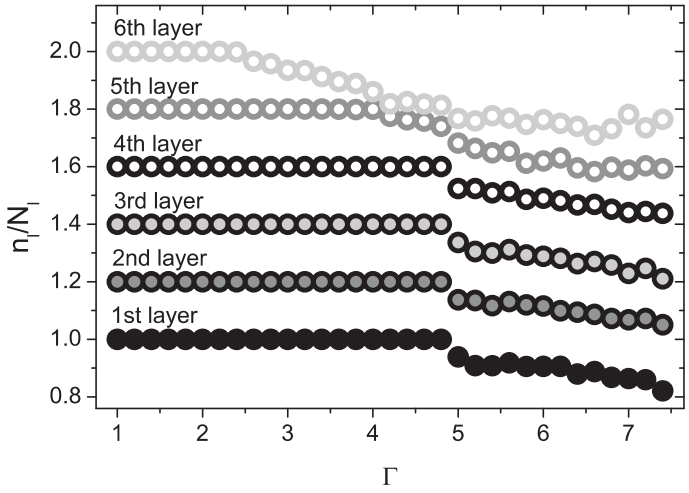

Figure 7.3: Normalized number of particles in the different layers as function of the normalized peak container acceleration Γ. For clarity the data for the layers two to six are shifted by $(l-1)\cdot 0.2$, where l is the number of the layer.

expansion continues and the layered structure becomes less and less pronounced.

More insight into the meltdown of the initial single crystal is gained by looking at the number of particles in the six lowest layers. A layer is defined as the region around a maximum in the density distribution. The boundaries are set halfway between neighboring local maxima. The lower boundary of the lowest layer is set at the same distance from the position of the corresponding maximum as the upper boundary of this layer. Equally the width of the sixth layer is assumed to be twice the distance between the position of the corresponding maximum and the lower layer boundary. Fig. 7.3 depicts the average number of particles per layer n_l normalized by the number of particles constituting the layer in the crystalline state N_l as a function of Γ. The number of particles in the sixth layer starts to drop at $\Gamma = 2.6$. The fifth layer lying below does not loose particles until Γ reaches a value of 4.2. What has been left of the crystal suddenly disintegrates at $\Gamma = 5.0$ leaving also the four lowest layers incomplete.

To characterize the dynamical behavior of the system the motion of single particles is monitored. Because of the high recording rate particles never travel farther than their own radius during the time between two consecutive images $\Delta t = 2\,\mathrm{ms}$. Therefore traces of all particles can be reconstructed. From this data the root mean square displacement of each particle in the horizontal Δx and vertical Δy direction, is calculated at delay times $\tau = k\Delta t$, according to the formulas

$$\Delta x\,(\tau) = \sqrt{\frac{1}{M-k}\sum_{i=1}^{M-k}\left(x_i - x_{i+k}\right)^2} \quad , \qquad \Delta y\,(\tau) = \sqrt{\frac{1}{M-k}\sum_{i=1}^{M-k}\left(y_i - y_{i+k}\right)^2}$$

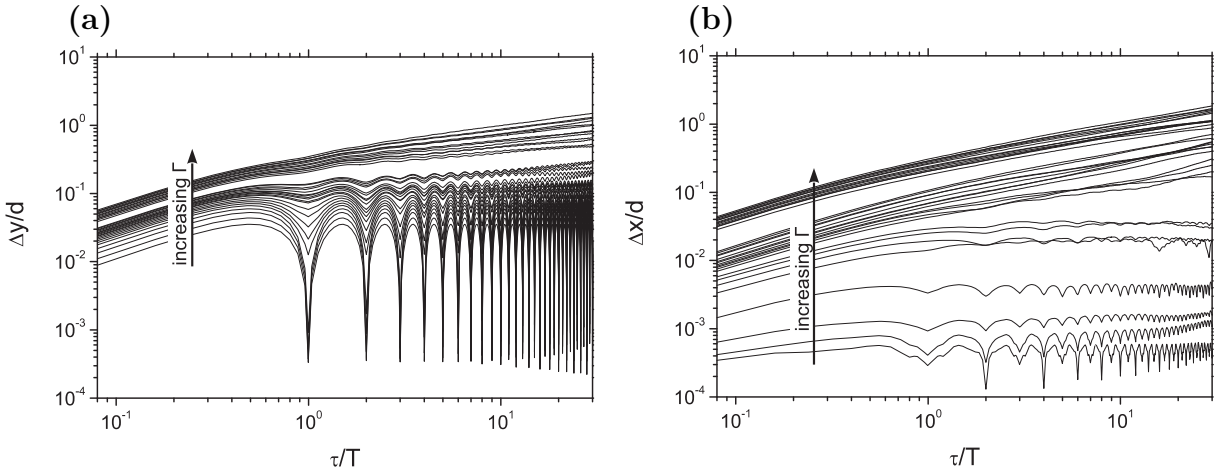

Figure 7.4: Root mean square displacement in the vertical (a) and horizontal (b) direction as a function of time for normalized peak container accelerations Γ between 1.0 and 7.4 in measured in steps of 0.2.

where (x_i, y_i) is the position of the particle in the ith image and M is the total number of images. The right hand side of these equation is nothing else but the square root of the structure function (Tatarski 1961). In Figs. 7.4a, b Δy and Δx, averaged over all traces and normalized by the particle diameter d, are plotted as functions of the dimensionless delay time τ/T, where T is the forcing period. The curves in Figs. 7.4a, b were interpolated around the extrema in order to avoid artifacts due to the finite sampling rate. For a given delay time the root mean square displacement increases with Γ. For low values of Γ the root mean square displacement in the vertical direction oscillates strongly at the forcing frequency, indicating that the container imposes its rhythm on the granular bed. Between the curves for $\Gamma = 4.8$ and $\Gamma = 5.0$ a gap appears. This surge of particle mobility coincides with the aforementioned disintegration of the close packing of the four lowest lying layers. At values of Γ above 5.0 the particles barely follow the container motion and its influence decreases steadily.

In the plot of the horizontal root mean square displacements the curves for values of Γ below the fluidization transition are also clearly separated from those belonging to values of Γ above it. Since horizontal movement of particles in the intact perfect crystal is virtually impossible, the root mean square displacement curves for $\Gamma < 2.6$ are almost constant. Only once the first particle pops up out of the sixth layer some particles have the possibility to travel horizontally, causing an increase of the root mean square displacement with delay time. Note that the periodic oscillations in the curves for the four lowest values of Γ are of very low amplitude (about 0.01 pixel), and therefore more likely due to a very slight tilt of the camera than real horizontal oscillations of the particles, especially since there should be no horizontal particle movement for $\Gamma = 1.0$.

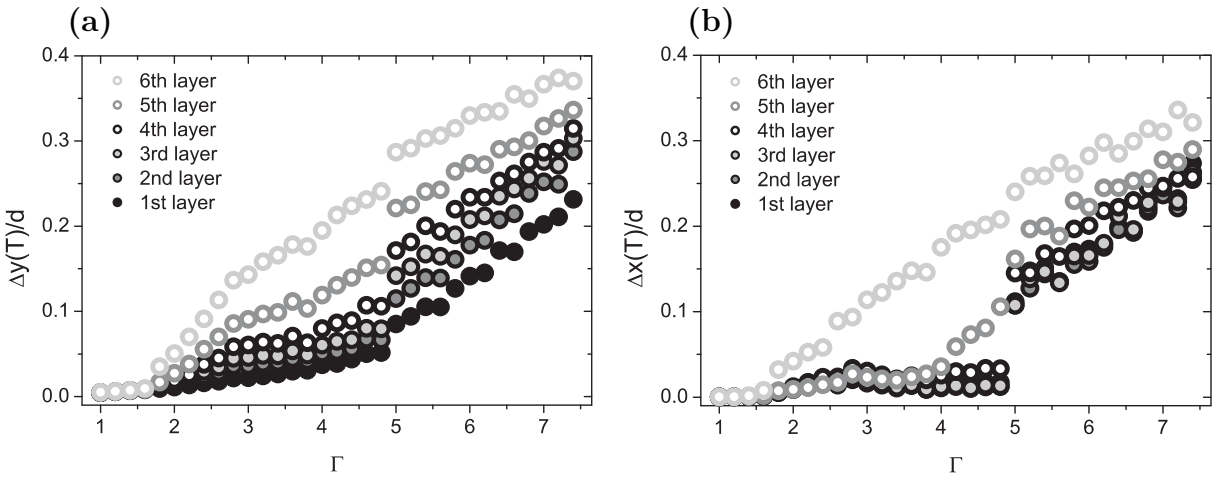

Figure 7.5: Root mean square displacement in the vertical (a) and horizontal (b) direction during one forcing period for particles in the six lowest layers.

After having examined the average dynamics of all particles the spatial dependence of particle motion is the next point to concentrate on. To obtain a reasonably high spatial resolution the bed is again divided into different layers. Figs. 7.5a, b show the root mean square displacement in the vertical and horizontal directions after a delay time of 26 ms, which is, allowing an error of 4 %, one forcing period, for the six lowest layers as a function of Γ. Up to $\Gamma = 1.6$ both the vertical and the horizontal root mean square displacements are close to zero for all layers. This means that the particles perform very regular trajectories returning to the same position after every driving period. At $\Gamma = 1.8$ the vertical root mean square displacements for particles in different layers split up. Even though for increasing Γ all curves rise and hence the particle trajectories deviate in general more and more from a simple periodic up and down motion, this trend is more pronounced for the upper layers. Between $\Gamma = 4.8$ and $\Gamma = 5.0$, once again, all curves feature a discontinuous jump. Above $\Gamma = 5.0$ the vertical root mean square displacement for particles in different layers tends to converge slightly with increasing forcing strength. The system becomes more homogeneous throughout its lower six layers.

Particles are only able to move horizontally once the layer to which they belong has got rid of some of its particles. This is not completely true for the top layer, because its leftmost and rightmost particles do not touch the side walls and therefore some wiggling motion is possible. This explains the increase in the horizontal root mean square displacement for the top layer between $\Gamma = 1.8$ and $\Gamma = 2.4$ even before the first particle leaves at $\Gamma = 2.6$, an event revealed by a relatively small step in the data. In contrast, the curve for the neighboring fifth layer does not rise until, at $\Gamma = 4.2$, the first particle is released. The horizontal root mean square displacement for the lower four layers remains close to zero up to $\Gamma = 4.8$, leaps up at $\Gamma = 5.0$ and increases steadily further on. Here again a trend

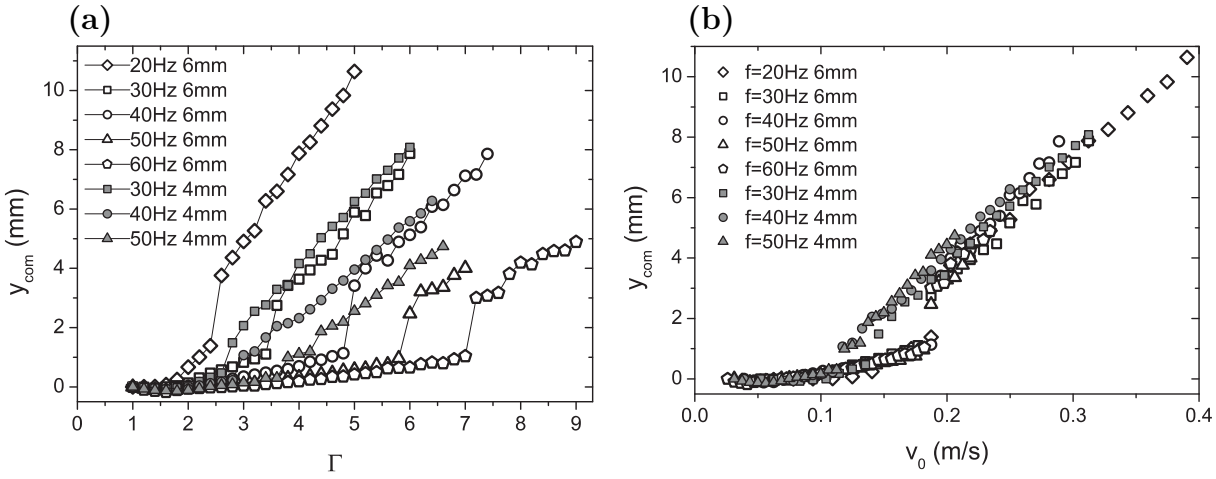

Figure 7.6: Height of the center of mass as a function of the normalized peak container acceleration Γ (a) and the maximum container velocity $v_0 = A(2\pi f)$ (b), for various frequencies and two different particle sizes.

to convergence can be observed above the fluidization transition of the lower four layers.

7.2.2 The center of mass height

Aiming to get a single quantity that characterizes the state of the system at a certain combination of forcing frequency and amplitude the average vertical center of mass position is calculated according to

$$y_{\mathrm{com}} = \frac{1}{MN} \sum_{i}^{M} \sum_{j}^{N} y_{ij} \quad ,$$

where y_{ij} is vertical position of the jth particle in the ith image and i and j run over the number of analyzed images M and the number of particles in the system N, respectively. The reference height is the minimum center of mass height possible which would be achieved if the particles were close packed and always stayed on the ground. In practice the vertical distances are measured with respect to the center of mass height for $\Gamma = 1.0$. For the system of the $N = 195$ glass beads with a diameter of 6 mm, driven at a frequency of 40 Hz, this quantity grows slightly until $\Gamma = 4.8$ (see Fig. 7.6a). As was already noticed in all previous plots a discontinuous transition takes place between $\Gamma = 4.8$ and $\Gamma = 5.0$. After that boost the center of mass height continues to grow steadily but more vigorously than below the transition point. Experiments at lower and higher driving frequencies result in curves with a similar trait, the main difference being a shift of the transition point towards higher values of Γ when the vibration frequency is raised and vice versa. In order to illuminate the influence of particle size the same experiments were also conducted with smaller glass particles that were only 4 mm in diameter. With these particles the difference

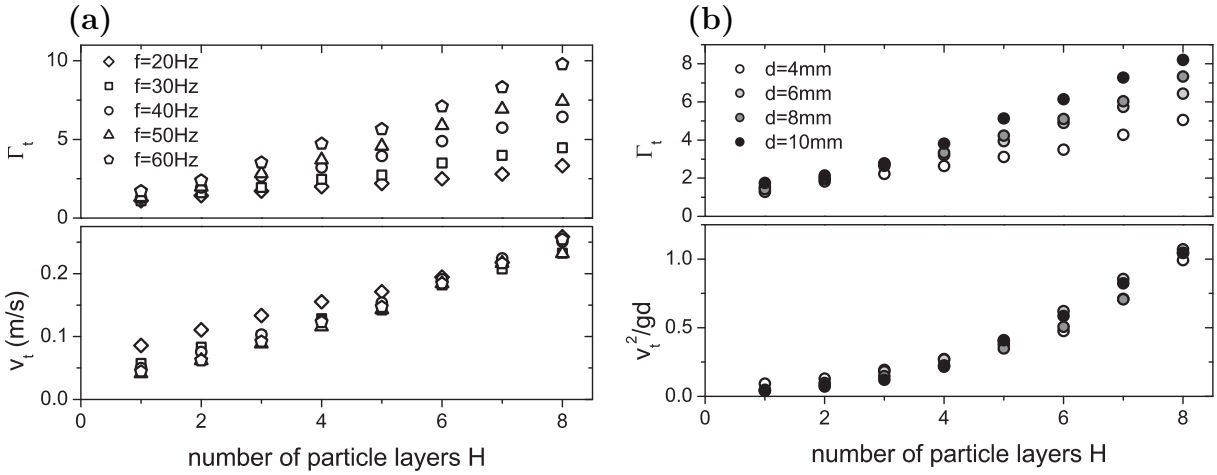

Figure 7.7: (a): Normalized peak container acceleration (top) and maximum container velocity (bottom) at the transition as a function of the number of particle layers for various frequencies. The particle diameter was kept constant at $d = 6\,\mathrm{mm}$. (b): Normalized peak container acceleration (top) and normalized squared maximum container velocity (bottom) at the transition as a function of the number of particle layers for various particle sizes. The driving frequency was fixed at $f = 40\,\mathrm{Hz}$.

in the center of mass height before and after the transition is considerably reduced. For the same driving frequencies the transition happens already at lower maximum container accelerations. However, at least when working at 30 and 40 Hz the center of mass height of the two particle sizes almost overlap once the system of larger particles has passed the transition point.

The data obtained for either particle size at different frequencies collapse when the center of mass height is plotted as a function of the maximum container velocity $v_0 = A(2\pi f) = g\Gamma/(2\pi f)$ (see Fig. 7.6b). Even if the transition for the two particle sizes occurs at different maximum container velocities all curves overlap fairly well below the transition point of the smaller particles and above the one for the larger particles.

For the particles with a diameter of 6.0 mm the values of Γ and v_0 where full fluidization occurs, Γ_t and v_t respectively, were measured as a function of the number of particle layers for various frequencies. Full fluidization is assumed when all layers have lost at least one particle compared to the perfect crystalline state. In accordance with Figs. 7.6a, b, Fig. 7.7a shows that for a given number of particle layers and the range of frequencies examined, the fluidization transition happens at a fixed value of v_0. Only for the smallest frequency and beds with less than five particle layers deviations from this scaling arise. The threshold velocity v_t increases almost linearly with increasing number of particle layers.

Fig. 7.7b shows Γ_t for glass particles of various size shaken at 40 Hz. A quite satisfactory

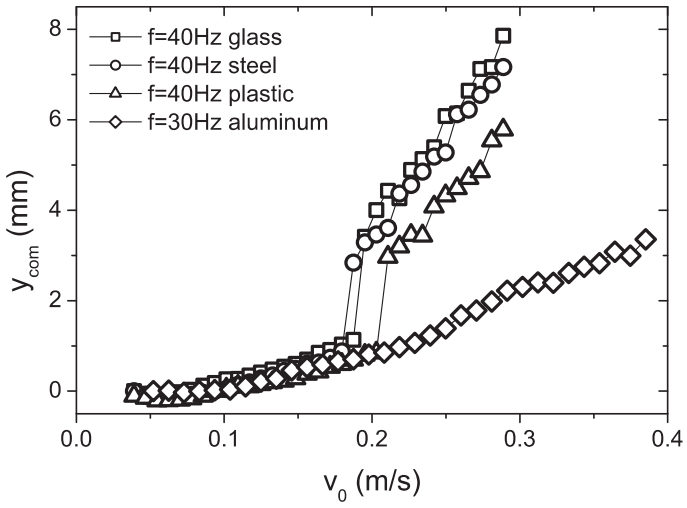

Figure 7.8: Height of the center of mass as a function of the maximum container velocity v_0 for four different materials. All particles have a diameter of 6 mm.

data collapse is reached for the Froude number $v_t^2/gd = \frac{1}{2}mv_t^2/mgr$, which is a measure for the amount of energy fed to a particle in proportion to the energy necessary to lift it by its own radius r. Pak and Behringer (1993) introduced this dimensionless kinetic energy as relevant parameter for the onset of a special type of surface waves.

The question arises how the particle *material* affects the results. Experiments were conducted using spherical steel, polyamide and aluminum particles to compare the results with those obtained for the glass beads. In Fig. 7.8 the center of mass heights for 6 mm particles made of four different materials are presented as functions of the maximum container velocity. While the curve for the steel particles lies only slightly below the one for the glass particles, the polyamide particles' center of mass is manifestly reduced for all values of v_0. Also the transition for the polyamide particles is shifted to higher maximum container velocities. The data for the aluminum particles show no transition at all. In order to attain higher maximum container velocities in the experiment with the aluminum particles the driving frequency was lowered. High speed movies reveal that the aluminum particles stay in close contact even at the highest forcing applied. Therefore the growth of the center of mass height for this system is solely due to higher jumps of the bed as a whole and not by its expansion. This behavior is explained by the fact that collisions involving aluminum particles are very inelastic as reflected by a low coefficient of restitution (compare Table 6.1 in Chapter 6). In general, the more elastic the material, the higher the center of mass for a given maximum container velocity.

Before starting the above described experiments a defect free crystal had been prepared manually. This was made possible by choosing the container width such that precisely an integer number of particles fit into the first layer. What happens if this is not the case?

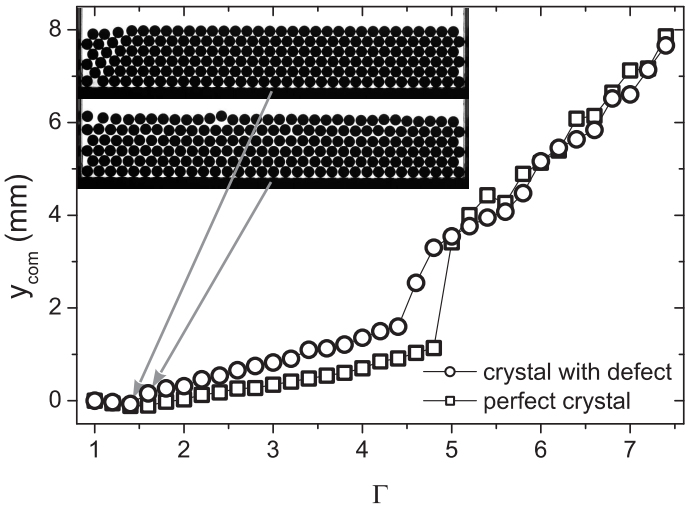

Figure 7.9: Height of the center of mass as a function of the normalized peak container acceleration Γ for two different initial packings. The particles are glass beads with a diameter of 6 mm and the vibration frequency is 40 Hz. The insets show snapshots of the defective crystal at $\Gamma = 1.4$ (top) and $\Gamma = 1.6$ (bottom).

To answer this question the box was broadened by two millimeters and the experiments with the 6 mm glass beads were repeated. The initial state had a localized defect close to the left sidewall as shown in the top inset of Fig. 7.9. This configuration remains stable up to $\Gamma = 1.4$. At $\Gamma = 1.6$ the defect spreads leading to a homogeneous crystal with slightly increased lattice spacing in the horizontal direction (see lower inset). For both systems the center of mass height indicates a transition at about the same value of Γ above which the data for the two experiments collapse. Note that, since the frequency in both cases was the same, equality of Γ also implies equality of v_0. As the center of mass height in the system with defect grows more rapidly when approaching the transition from below than in the case of an initially perfect crystal the subsequent jump is less pronounced. Decreasing the maximum container velocity below the transition in general does not restore a perfect crystalline structure but leaves some defects behind. In order to grow a single crystal the particles would have to be added one after another under constant modest vibration at slow feeding rate (Nahmad-Molinari and Ruiz-Suárez 2002).

7.3 Summary and conclusion

In the preceding sections experiments on vertically vibrated two-dimensional granular packings have been presented. A discontinuous transition between a partly crystalline state and a completely fluidized state occurs at a fixed value of v_0^2/dg for a given number of particle layers. When the number of particle layers increases the fluidization threshold

also increases. The transition is characterized by a sudden bed expansion and a surge of particle displacements. As a consequence, at the transition the center of mass height increases by leaps and bounds. In the fully fluidized state the maximum container velocity v_0 is the crucial driving parameter that determines the center of mass height. The discontinuity of the transition turned out to be less pronounced when smaller particles were used. If the experiments are started with a defective close packing instead of a perfect monocrystalline structure the rise of the center of mass height at the transition becomes less sharp. A fluidization transition could only be observed when the particles were not too inelastic. A bed of aluminum particles did not fluidize even for the highest forcing accessible. Even though the bed deforms during flight phases and exhibits bending waves, the particles always stay in close contact and the crystalline structure is largely preserved.

Olafsen and Urbach (2005) and Reis et al. (2006) studied the melting of a horizontal monolayer of spheres confined between two vibrating plates and found a continuous transition from a hexagonally ordered solid phase to a disordered liquid. Here it is shown that a vibrated two-dimensional vertical packing of spheres exhibits a discontinuous fluidization transition from a crystalline state, in which only particles close to the surface are mobile, to a fully fluidized state. Surface melting preceding the phase transition in the bulk is already known from many classes of solids (for a review see Dash et al. (1995)). However the fluidization transition is first order as predicted for grain-boundary melting in two dimensions by Chui (1982). The scenario of a gradually shrinking solid fraction, put forward by Quinn and Hong (2000), is therefore not true for two- dimensional vertical packings driven by an oscillating container.

Thus the fluidization transition in granular assemblies confined to two-dimensions may be continuous or discontinuous depending on whether the directions of gravity and forcing are perpendicular or parallel to the plane of confinement.

For all fluidization transitions presented in this chapter the driving frequency was considerably higher than the crossover frequency f_d, above which Mujica and Melo (2000) claimed that a fluidization transition would not happen. For a granular bed consisting of six particle layers $f_{4\,\mathrm{mm}} = 20.2\,\mathrm{Hz}$ with the smaller particles and $f_{6\,\mathrm{mm}} = 16.5\,\mathrm{Hz}$ with the larger ones. Instead of a fluidization transition these authors reported the appearance of small amplitude bending waves in the high frequency regime. In the presented experiments bending waves, which are called 'undulations' by Sano (2005), have only been observed when using very inelastic aluminum particles. Furthermore the solid-liquid-type transition found by Mujica and Melo in the low frequency regime occurred at fixed $\Gamma \approx 2.0$, in contrast to one of the main results of this work, the finding that the Froude number v_0^2/gd is the decisive quantity.

For three-dimensional systems of randomly packed particles surface heaping caused by

convection has been reported by Evesque and Rajchenbach (1989), Laroche et al. (1989), and Wassgren et al. (1996) to set in at a critical peak container acceleration close to $1.2\,g$. Such convective particle flow below the onset of full fluidization is suppressed here by the close particle packing. Reynolds (1885) already observed that voids are essential to allow particles to flow in the first place. In addition, the particles used in the experiments are larger than the ones used by the above mentioned authors. The influence of sidewall friction, one of the driving mechanisms for convection (Clément et al. 1992), will decrease with increasing particle weight compared to gravitational forces and forces transmitted via the oscillating container floor. Thus the lack of convection may also be due to the larger particle size in the experiments presented in this chapter. Furthermore Laroche pointed out that in his experiments convective particle motion was only seen in deep beds with more than 10 particle layers. The size of the used particles also lies well above 1 mm, the size below which the surrounding gas starts to play a bigger role in the formation of convection cells leading to Faraday heaping (Faraday 1831; Pak et al. 1995; Thomas and Squires 1998).

It remains an open question whether the fluidization transition of three-dimensional ordered packings is also discontinuous, the scaling properties of those systems still have to be explored.

Chapter 8

Conclusion and Outlook

In summary, three phenomena occurring in circularly vibrated granular beds have been examined, namely extended subharmonic surface waves, pulses of localized subharmonic waves, and solid/fluid coexistence. The overview Fig. 8.1 shows where these phenomena are located in the two-dimensional parameter space, spanned by the number of particle layers H_0 and the forcing strength Γ. In an additional experiment the fluidization transition of a vertically vibrated, two-dimensional hard sphere packing has been studied.

Circular vibration results in material transport which is responsible for the drift of subharmonic waves and the motion of phase boundaries between solid and fluid regions. The nonlinear dependence of the transport velocity at fixed forcing parameters on the amount of material in the container leads to the formation of pulses of subharmonic waves.

The extended subharmonic surface waves treated in Chapter 3 appear in the range $2.4 < \Gamma < 4.8$. It remains an open question how the pattern sets in and how it disappears. The transitions from the unstructured to the structured state might be subcritical or supercritical. In the case of a subcritical bifurcation one could hope to find localized solitary waves in the hysteretic region, similar to the "oscillons" discovered by Umbanhowar et al. (1996).

The question how the wavelength of extended subharmonic waves depends on the vibration amplitude has not yet been answered satisfactorily. Preliminary measurements at amplitudes of 1.4, 1.7, and 2.1 mm indicate that the wavelengths collapse when plotted as a function of Γ, but data is too scarce to allow a definitive statement.

Furthermore, the dependence of the wave pattern on the bed thickness has not yet been studied systematically. For the vibration settings of Chapter 4, resulting in a normalized peak forcing acceleration of $\Gamma = 5.6$, waves only appear for beds thicker than $H_0 = 8.5$. It has been verified that such a minimum bed thickness also exists for extended surface waves described in Chapter 3. The question how the wavelength and the critical values of Γ for wave onset above the minimum bed thickness change with the amount of material

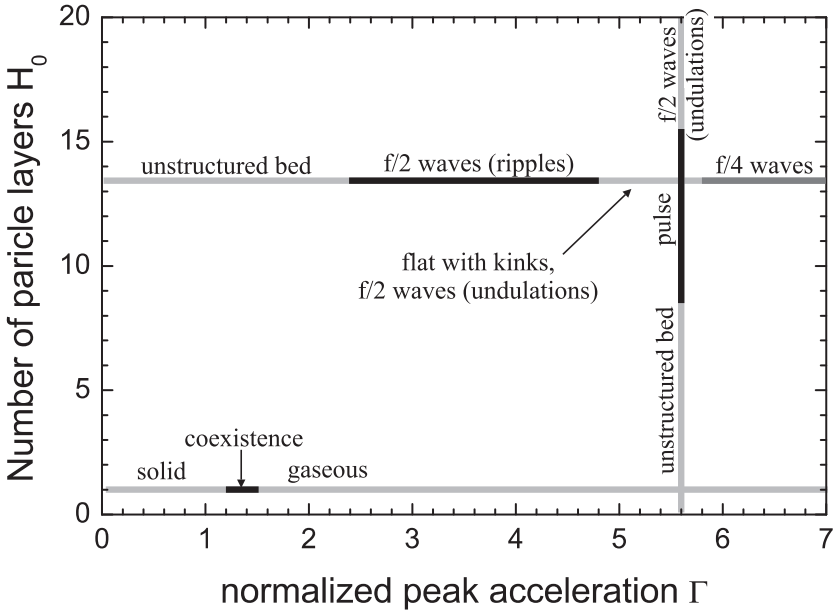

Figure 8.1: Structure formation phenomena of granular matter in an annular container upon circular vibration. The regions in parameter space covered by the experiments described in Chapters 3, 4 and 5 are indicated by the black and gray lines.

in the container is left for future investigations.

Note that the subharmonic waves described in Chapter 4 occur at stronger forcing than the extended surface waves Chapter 3 deals with. In the first case the whole bed is undulated while in the latter case waves appear only at the surface, while the bed floor remains flat. Sano (2005) calls the waves appearing in these two cases "undulations" and "ripples", respectively.

On the theory side the continuum description for circularly vibrated sand by Grevenstette and Linz (2006) needs to be improved. In its present state it only qualitatively reproduces the experimentally observed wave pattern, namely drifting subharmonic waves. It remains to be seen whether the model can be improved so that it yields the experimentally measured drift velocity and wavelength as functions of Γ.

As in vertically vibrated beds (Bizon et al. 1998), waves oscillating at one quarter of the driving frequency have been observed for $\Gamma > 5.8$. A detailed investigation was abandoned for fear of overstraining the machinery which, in this regime, is working at the upper limit of attainable accelerations. Although an exact comparison between patterns obtained with and without horizontal oscillation component is still missing, it seems that the main difference of the structures seen for circular vibration compared to those for pure vertical vibration is the pattern drift at the transport velocity.

Beside the question about the bifurcation type of the wave instability in the annular

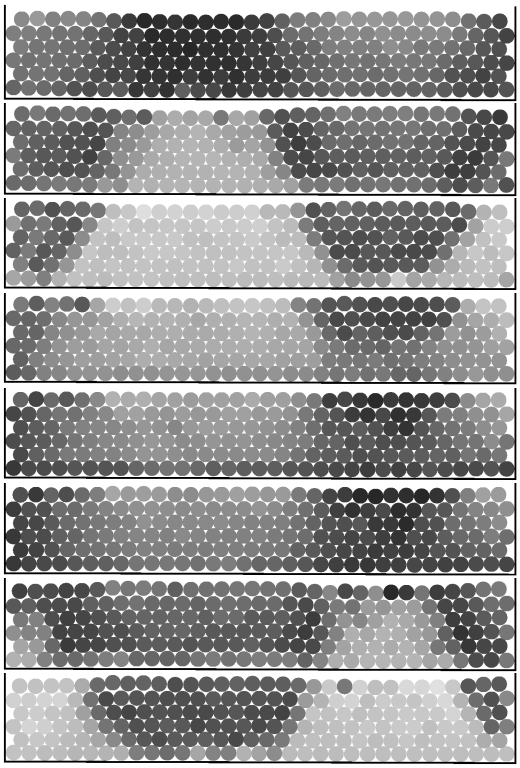

Figure 8.2: Small amplitude waves in a bed of aluminum spheres ($d = 6\,\mathrm{mm}$). Time increases from top to bottom in steps of 4.0 ms or 0.2 driving periods between successive images. The driving frequency is 50 Hz and the normalized peak container acceleration is $\Gamma = 4.0$. Particles are drawn in gray scale according to their vertical velocity. The brighter a particle the higher its velocity (Velocities in the upward direction are counted positive).

container, the nature of the subharmonic wave onset for the two-dimensional packing of highly inelastic aluminum spheres under pure vertical vibration (see Chapter 6) is still unresolved. From experiments with the same setup as used for the fluidization of a two-dimensional hard sphere packing the particle velocities in the vertical direction were extracted (see Fig. 8.2). Averaged over vertical slices and plotted as a function of the horizontal position they clearly reflect the transition from uniform oscillations to a standing wave pattern. First preliminary results indicate a supercritical, nonhysteretic transition from the flat, unstructured to the wavy state. This work is still in progress.

In Chapter 4 the shape of the fundamental diagram, which expresses the relation between transport velocity and bed thickness, remains unexplained. Collisions of thick beds with the container floor are completely inelastic. Hence their transport velocity can be predicted from simulations where the granular bed is modeled as a single plastic object with appropriate friction coefficient. In contrast, highly fluidized thin beds are transported

in the opposite direction and the transport velocity decreases when the bed thickness is reduced. The key to understand this intriguing behavior probably lies in the collision statistics of particle-container impacts. It would be very helpful to know how the collisions between particle and container are distributed throughout a driving cycle and how much horizontal momentum is transferred on average in a collision at any given phase of the driving. Molecular dynamics simulations would be well suited to answer these questions.

A further challenge, waiting to be tackled, is the development of a continuum model that explains the phenomenon of solid/fluid coexistence. To set up such a model, the mechanism that keeps the boundaries between the solid and fluid regions at a constant distance has to be identified. A first step in this direction would be to examine the particle fluxes across the boundary from the fluid to the solid region and vice versa, which could already be done by analyzing the data obtained from the performed molecular dynamics simulations. The loading range where coexistence of solid and fluid regions occurs has not yet been examined in detail. Checks made for loads of 0.5 and 2.0 particle layers showed that the phenomenon persists in these cases. For 3.0 particle layers no lateral phase separation was obvious to the eye. So it seems that thicker beds fluidize from top to bottom while in thin beds up to approximately three particle layers locally nucleated fluidized regions grow laterally. More experiments are necessary to make reliable statements.

Both the occurrence of localized subharmonic waves and the coexistence of gas and solid are intimately connected with the fluidization transition. This was the motivation to study the way a granular packing fluidizes and how this transition is influenced by the parameters of driving and particles. Unfortunately it was not possible with the available equipment to track individual particles in a three-dimensional system. Therefore a new container was designed that confined the particles to two dimensions. Because of the rectangular container geometry lateral material transport could not be sustained and the container oscillation was restricted to the vertical direction. Whether the fluidization transition in the quasi two-dimensional annular channel system shows the same features remains an open question. Also the influence of the additional horizontal oscillation component on the state of fluidization is left for future investigations.

A recently completed annular container that can be evacuated opens up the possibility to examine the influence of interstitial air on vibrated powders. According to Pak et al. (1995) for granular beds consisting of particles with a diameter $d = 1\,\mathrm{mm}$, as used for the experiments with the annular vibration apparatus, the surrounding fluid has virtually no effect unless the bed thickness becomes larger than 10 cm. But when smaller particles are used the interstitial air has already to be taken into account for much thinner beds, generating effects like convection accompanied by heaping (Thomas and Squires 1998)

and bubbling, i.e. the formation and upward motion of voids (Pak and Behringer 1994). Numerous investigations into the segregation of binary particle mixtures have revealed interesting structure formation phenomena. On the one hand there is the Brazil-nut effect and its reverse for vertical vibration (Breu, Ensner, Kruelle, and Rehberg 2003), i.e. the vertical segregation of particles of different size and/or density. On the other hand in horizontally vibrated monolayers of binary mixtures clusters consisting of only one type of grains were discovered by Reis et al. (2002, 2004). Under certain conditions these clusters form stripes of well defined width and interstripe distance. Both effects are expected to show up when granular matter is vibrated circularly. Experiments to investigate these structure formation phenomena in binary (sub)monolayers are planned for the near future.

References

Alexeev, A., V. Royzen, V. Dudko, A. Goldshtein, and M. Shapiro (1999). Dynamics of vertically vibrated two-dimensional granular layers. *Phys. Rev. E 59*, 3231–3241.

Anderson, K. E. and R. P. Behringer (1990). Long-time scales in traveling-wave convection patterns. *Phys. Lett. A 145*, 323–328.

Aranson, I. S., D. Blair, V. A. Kalatsky, G. W. Crabtree, W.-K. Kwok, V. M. Vinokur, and U. Welp (2000). Electrostatically driven granular media: Phase transitions and coarsening. *Phys. Rev. Lett. 84*, 3306–3309.

Aranson, I. S. and L. S. Tsimring (2006). Patterns and collective behavior in granular media: Theoretical concepts. *Rev. Mod. Phys. 78*, 641.

Bagnold, R. A. (1941). *The physics of blown sand and desert dunes*. Morrow.

Bak, P., C. Tang, and K. Wiesenfeld (1987). Self-organized criticality: An explanation of the 1/f noise. *Phys. Rev. Lett. 59*, 381–384.

Barrat, A. and E. Trizac (2002). Lack of energy equipartition in homogeneous heated binary granular mixtures. *Granular Matter 4*, 57.

Barten, W., M. Lücke, and M. Kamps (1991). Localized traveling-wave convection in binary-fluid mixtures. *Phys. Rev. Lett. 66*, 2621–2624.

Barten, W., M. Lücke, M. Kamps, and R. Schmitz (1995). Convection in binary fluid mixtures. ii. localized traveling waves. *Phys. Rev. E 51*, 5662–5680.

Bernstein, A. D. (1977). Listening to the coefficient of restitution. *Am. J. Phys. 45*, 41.

Bizon, C., M. D. Shattuck, J. B. Swift, W. D. McCormick, and H. L. Swinney (1998). Patterns in 3d vertically oscillated granular layers: simulation and experiment. *Phys. Rev. Lett. 80*, 57–60.

Breu, A. P. J., H.-M. Ensner, C. A. Kruelle, and I. Rehberg (2003). Reversing the brazil-nut effect: competition between percolation and condensation. *Phys. Rev. Lett. 90*, 014302.

Campbell, C. S. (1990). Rapid granular flows. *Annu. Rev. Fluid Mech. 22*, 57–92.

Chladni, E. F. F. (1787). *Entdeckungen über die Theorie des Klanges*. Leipzig: Breitkopf und Härtel.

Chui, S. T. (1982). Grain-boundary theory of melting in two dimensions. *Phys. Rev. Lett. 48*, 933–935.

Clément, E., J. Duran, and J. Rajchenbach (1992). Experimental study of heaping in a two-dimensional sandpile. *Phys. Rev. Lett. 69*, 1189–1192.

Clément, E. and J. Rajchenbach (1991). Fluidization of a bidimensional powder. *Europhys. Lett. 16*, 133–138.

Clément, E., L. Vanel, J. Rajchenbach, and J. Duran (1996). Pattern formation in a vibrated granular layer. *Phys. Rev. E 53*, 2972–2975.

Dash, J. G., H.-Y. Fu, and J. Wettlaufer (1995). The premelting of ice and its environmental consequences. *Rep. Prog. Phys. 58*, 115–167.

de Coulomb, C.-A. (1785). Théorie des machines simples, en ayant égard au frottement de leurs parties et á la roideur des cordages. In *Memoires de mathématique et de physique présentées á l'Académie Royale des Sciences par divers Savants*, Volume 10, pp. 161–332.

de Gennes, P. G. (1999). Granular matter: a tentative view. *Rev. Mod. Phys. 71*(2), S374–S382.

Dennin, M., G. Ahlers, and D. S. Cannell (1996). Chaotic localized states near the onset of electroconvection. *Phys. Rev. Lett. 77*, 2475–2478.

Douady, S., S. Fauve, and C. Laroche (1989). Subharmonic instabilities and defects in a granular layer under vertical vibration. *Europhys. Lett. 8*, 621–627.

Eggers, J. (1999). Sand as maxwell's demon. *Phys. Rev. Lett. 83*(25), 5322–5325.

Eggers, J. and H. Riecke (2006). Continuum description of vibrated sand. *Phys. Rev. E 59*, 4476–4483.

Eisenmann, C., U. Gasser, P. Keim, and G. Maret (2004). Anisotropic defect-mediated melting of two-dimensional colloidal crystals. *Phys. Rev. Lett. 93*, 105702.

El hor, H. and S. J. Linz (2005). Model for transport of granular matter on an annular vibratory conveyor. *J. Stat. Mech.*, L02005.

El hor, H., S. J. Linz, R. Grochowski, P. Walzel, C. A. Kruelle, M. Rouijaa, A. Götzendorfer, and I. Rehberg (2005). Modol for transport of granular matter on vibratory conveyors. In García-Rojo, Herrmann, and McNamara (Eds.), *PG05*, Rotterdam, pp. 1191–1195. Balkema.

Eshuis, P., K. van der Weele, D. van der Meer, and D. Lohse (2005). Granular leidenfrost effect: experiment and theory of floating particle clusters. *Phys. Rev. Lett. 95*, 258001.

Evesque, P. and J. Rajchenbach (1989). Instability in a sand heap. *Phys. Rev. Lett. 62*, 44–46.

Evesque, P., E. Szmatula, and J.-P. Denis (1990). Surface fluidization of a sand pile. *Europhys. Lett. 12*, 623–627.

Falcon, É., S. Fauve, and C. Laroche (1999). Cluster formation, pressure and density measurements in a granular medium fluidized by vibrations. *Eur. Phys. J. B 9*, 183–186.

Faraday, M. (1831). On a peculiar class of acoustical figures. *Phil. Trans. R. Soc. Lond. 121*, 299.

Farkas, I., D. Helbing, and T. Vicsek (2002). Mexican waves in an excitable medium. *Nature 419*, 131–132.

Feitosa, K. and N. Menon (2002). Breakdown of energy equipartition in a 2d binary vibrated granular gas. *Phys. Rev. Lett. 88*(19), 198301.

Gallas, J. A. C., H. J. Herrmann, and S. Sokołowski (1992). Molecular dynamics simulation of powder fluidization in two dimensions. *Physica A 189*, 437–446.

Götzendorfer, A., J. Kreft, C. A. Kruelle, and I. Rehberg (2005). Sublimation of a vibrated granular monolayer: coexistence of gas and solid. *Phys. Rev. Lett. 95*, 135704.

Götzendorfer, A., C. A. Kruelle, and I. Rehberg (2005). Granular surface waves in a vibratory conveyor. In García-Rojo, Herrmann, and McNamara (Eds.), *PG05*, Rotterdam, pp. 1181–1184. Balkema.

Götzendorfer, A., D. Svenšek, C. A. Kruelle, and I. Rehberg (2006). Localized subharmonic waves in a circularly vibrated granular bed. submitted to Phys. Rev. Lett.

Götzendorfer, A., C.-H. Tai, C. A. Kruelle, I. Rehberg, and S.-S. Hsiau (2006). Fluidization of a vertically vibrated two-dimensional hard sphere packing: A granular meltdown. *Phys. Rev. E 74*, 011304.

Grevenstette, M. and S. Linz (2006). Continuum modeling of granular surface structures on vibratory conveyors. In R. Grochowski, C. A. Kruelle, S. Linz, and P. Walzel (Eds.), *Behavior of granular media*. Shaker.

Grochowski, R., S. Strugholtz, H. El hor, S. J. Linz, and P. Walzel (2004). Transport properties of granular matter on vibratory conveyors. In S. E. Pratsinis, H. Schulz,

R. Strobel, and C. Schreglmann (Eds.), *PARTEC 2004*.

Grochowski, R., P. Walzel, M. Rouijaa, C. A. Kruelle, and I. Rehberg (2004). Reversing granular flow on a vibratory conveyor. *Appl. Phys. Lett. 84*, 1019–1021.

Hawes, I., A.-M. Schwartz, D. Sutherland, and C. Howard-Williams (2003). Aquatic ecosystems of the mcmurdo dry valleys - the edge of survival. *Water & Atmosphere 11*, 16–17.

Helal, K., T. Biben, and J. P. Hansen (1997). Local fluctuations in a fluidized granular medium. *Physica A 240*, 361–373.

Helbing, D. (2001). Traffic and related self-driven many-particle systems. *Rev. Mod. Phys. 73*, 1067–1141.

Herminghaus, S. (2005). Dynamics of wet granular matter. *Adv. Phys. 54*, 221–261.

Hongler, M.-O., P. Cartier, and P. Flury (1989). Numerical study of a model of vibro-transporter. *Phys. Lett. A 135*, 106–112.

Huntley, J. M. (1998). Scaling laws for a two-dimensional vibro-fluidized granular material. *Phys. Rev. E 58*, 5168–5170.

Jaeger, H. M., S. R. Nagel, and R. P. Behringer (1996). Granular solids, liquids, and gases. *Rev. Mod. Phys. 68*(4), 1259–1273.

Jähne, B. (2002). *Digital image processing*. Berlin: Springer.

Jaster, A. (1999). Computer simulations of the two-dimensional melting transition using hard disks. *Phys. Rev. E 59*, 2594–2602.

Jung, D. and M. Lücke (2002). Localized waves without the existence of extended waves: oscillatory convection of binary fluid mixtures with strong soret effect. *Phys. Rev. Lett. 89*, 054502.

Kadanoff, L. P. (1999). Built upon sand: Theoretical ideas inspired by granular flows. *Rev. Mod. Phys. 71*(1), 435–444.

Kerner, B. S. and P. Konhäuser (1993). Cluster effect in initially homogeneous traffic flow. *Phys. Rev. E 48*, R2335–R2338.

Kolodner, P. (1991). Drifting pulses of traveling-wave convection. *Phys. Rev. Lett. 66*, 1165–1168.

Kolodner, P., D. Bensimon, and C. M. Surko (1988). Traveling-wave convection in an annulus. *Phys. Rev. Lett. 60*, 1723–1726.

Kruelle, C. A., S. Aumaître, A. P. J. Breu, A. Götzendorfer, T. Schnautz, R. Grochowski, and P. Walzel (2004). Phase transitions and segregation phenomena in vibrated granular systems. *Adv. in Solid State Phys. 44*, 401–414.

Kruelle, C. A., M. Rouijaa, A. Götzendorfer, I. Rehberg, R. Grochowski, P. Walzel, H. El hor, and S. J. Linz (2005). Reversal of a granular flow on a vibratory conveyor. In García-Rojo, Herrmann, and McNamara (Eds.), *PG05*, Rotterdam, pp. 1185–1189. Balkema.

Kudrolli, A. (2004). Size separation in vibrated granular matter. *Rep. Prog. Phys. 67*, 209–247.

Kurtze, D. A. and D. C. Hong (1995). Traffic jams, granular flow, and soliton selection. *Phys. Rev. E 52*, 218–221.

Kusner, R. E., J. A. Mann, J. Kerins, and A. J. Dahm (1994). Two-stage melting of a two-dimensional collodial lattice with dipole interactions. *Phys. Rev. Lett. 73*, 3113–3116.

Landwehr, F., R. Lange, and P. Walzel (1997). Partikeltransport unter verschiedenen stoßbedingungen auf vibrierten unterlagen. *Chem. Ing. Tech. 69*, 1422–1426.

Landwehr, F. and P. Walzel (1999). Simulation von partikelbewegung auf vibrierten unterlagen. *Chem. Ing. Tech. 71*, 1167–1170.

Laroche, C., S. Douady, and S. Fauve (1989). Convective flow of granular masses under vertical vibrations. *J. Phys. France 50*, 699–706.

Lioubashevski, O., H. Arbell, and J. Fineberg (1996). Dissipative solitary states in driven surface waves. *Phys. Rev. Lett. 76*, 3959–3962.

Lioubashevski, O., Y. Hamiel, A. Agnon, Z. Reches, and J. Fineberg (1999). Oscillons and propagating solitary waves in a vertically vibrated colloidal suspension. *Phys. Rev. Lett. 83*, 3190–3193.

Losert, W., D. G. W. Cooper, and J. P. Gollub (1999). Propagating front in an excited granular layer. *Phys. Rev. E 59*, 5855–5861.

Luck, J. M. and A. Mehta (1993). Bouncing ball with a finite restitution: chattering, locking, and chaos. *Phys. Rev. E 48*, 3988.

Luding, S., H. J. Herrmann, and A. Blumen (1994). Simulations of two-dimensional arrays of beads under external vibrations: Scaling*Phys. Rev. E 50*, 3100–3108.

Mehta, A. and G. C. Barker (1994). The dynamics of sand. *Rep. Prog. Phys. 57*, 383–416.

Melo, F., P. Umbanhowar, and H. L. Swinney (1994). Transitions to parametric wave patterns in a vertically oscillated granular layer. *Phys. Rev. Lett. 72*, 172–175.

Melo, F., P. Umbanhowar, and H. L. Swinney (1995). Hexagons, kinks, and disorder in oscillated granular layers. *Phys. Rev. Lett. 75*, 3838–3841.

Metcalf, T. H., J. B. Knight, and H. M. Jaeger (1997). Standing wave patterns in shallow beds of vibrated granular material. *Physica A 236*, 202–210.

Mitarai, N. and F. Nori (2006). Wet granular materials. *Adv. Phys. 55*, 1–45.

Moriyama, O., N. Kuroiwa, M. Matsushita, and H. Hayakawa (1998). 4/3 law of granular particles flowing through a vertical pipe. *Phys. Rev. Lett. 80*, 2833–2836.

Mujica, N. and F. Melo (2000). Experimental study of solid-liquid-type transitions in vibrated granular layers and the relation with surface waves. *Phys. Rev. E 63*, 011303.

Murray, C. A. and D. H. VanWinkle (1987). Experimental observation of two-stage melting in a classical two-dimensional screened coulomb system. *Phys. Rev. Lett. 58*, 1200–1203.

Nagatani, T. (2002). The physics of traffic jams. *Rep. Prog. Phys. 65*, 1331–1386.

Nagel, S. R. (1992). Instabilities in a sandpile. *Rev. Mod. Phys. 64*(1), 321–325.

Nahmad-Molinari, Y. and J. C. Ruiz-Suárez (2002). Epitaxial growth of granular single crystals. *Phys. Rev. Lett. 89*, 264302.

Nie, X., E. Ben-Naim, and S. Y. Chen (2000). Dynamics of vibrated granular monolayers. *Europhys. Lett. 51*, 679–684.

Niemela, J. J., G. Ahlers, and D. S. Cannell (1990). Localized traveling-wave states in binary-fluid convection. *Phys. Rev. Lett. 64*, 1365–1368.

Olafsen, J. S. and J. S. Urbach (1998). Clustering, order, and collapse in a driven granular monolayer. *Phys. Rev. Lett. 81*, 4369–4372.

Olafsen, J. S. and J. S. Urbach (2005). Two-dimensional melting far from equilibrium in a granular monolayer. *Phys. Rev. Lett. 95*, 098002.

Pak, H. K. and P. R. Behringer (1994). Bubbling in vertically vibrated granular materials. *Nature 371*, 231–233.

Pak, H. K. and R. P. Behringer (1993). Surface waves in vertically vibrated granular materials. *Phys. Rev. Lett. 71*, 1832.

Pak, H. K., E. Van Doorn, and R. P. Behringer (1995). Effects of ambient gases on granular materials under vertical vibration. *Phys. Rev. Lett. 74*, 4643–4646.

Pöschel, T. and S. Luding (Eds.) (2001). *Granular gases*. Berlin: Springer.

Prevost, A., P. Melby, D. A. Egolf, and J. S. Urbach (2004). Nonequilibrium two-phase coexistence in a confined granular layer. *Phys. Rev. E 70*, 050301(R).

Quinn, P. V. and D. C. Hong (2000). Liquid-solid transition of hard spheres under gravity. *Phys. Rev. E 62*, 8295–8298.

Quinn, R. A. and J. Goree (2001). Experimental test of two-dimensional melting throug disclination unbinding. *Phys. Rev. E 64*, 051404.

Rademacher, F. J. S. (1995). On the theoretical and experimental conveying speed of granular bulk solids on vibratory conveyors. *Bulk Solids Handling 15*, 41.

Rademacher, F. J. S. and L. Ter Borg (1994). On the theoretical and experimental conveying speed of granular bulk solids on vibratory conveyors. *Forschung im Ingenieurwesen - Engineering Research 60*, 261.

Reis, P. M., G. Ehrhardt, A. Stephenson, and T. Mullin (2004). Gases, liquids and crystalls in granular segregation. *Europhys. Lett. 66*, 357–363.

Reis, P. M., R. A. Ingale, and M. D. Shattuck (2006). Crystallization of a quasi-two-dimensional granular fluid. *Phys. Rev. Lett. 96*, 258001.

Reis, P. M. and T. Mullin (2002). Granular segregation as a critical phenomenon. *Phys. Rev. Lett. 89*, 244301.

Reynolds, O. (1885). On the dilatancy of media composed of rigid particles in contact. *Philos. Mag. 20*, 469.

Riecke, H. (1992). Self-trapping of traveling-wave pulses in binary mixture convection. *Phys. Rev. Lett. 68*, 301–304.

Riecke, H. and G. D. Granzow (1998). Localization of waves without bistability: Worms in nemactic electroconvection. *Phys. Rev. Lett. 81*, 333–336.

Ristow, G. H., G. Straßburger, and I. Rehberg (1997). Phase diagram and scaling of granular materials under horizontal vibrations. *Phys. Rev. Lett. 79*, 833–836.

Rouijaa, M., C. A. Kruelle, I. Rehberg, R. Grochowski, and P. Walzel (2005). Transport and pattern formation in granular materials on a vibratory conveyor. *Chem. Eng. Technol. 28*, 41–44.

Sano, O. (2005). Dilatancy, buckling, and undulations on a vertically vibrating granular layer. *Phys. Rev. E 72*, 051302.

Sapozhnikov, M. V., I. S. Aranson, and J. S. Olafsen (2003). Coarsening of granular clusters: Two types of scaling behaviors. *Phys. Rev. E 67*, 010302(R).

Schlichting, H. J. and V. Nordmeier (1996). Strukturen im sand: Kollektives verhalten und selbstorganisation bei granulaten. *Math. Naturwiss. Unterr. 49*, 323.

Sengupta, S., P. Nielaba, and K. Binder (2000). Elastic moduli, dilocation core energy, and melting of hard disks in two dimensions. *Phys. Rev. E 61*, 6294–6301.

Sloot, E. M. and N. P. Kruyt (1996). Theoretical and experimental study of the transport of granular materials by inclined vibratory conveyors. *Powder Technol. 87*, 203.

Smith, P. A., C. D. Spencer, and D. E. Jones (1981). Microcomputer listens to the coefficient of restitution. *Am. J. Phys. 49*, 136.

Stensgaard, I. and E. Lægsgaard (2001). Listening to the coefficient of restitution - revisited. *Am. J. Phys. 69*, 301.

Strandburg, K. J. (1988). Two-dimensional melting. *Rev. Mod. Phys. 60*, 161–207.

Tai, C.-H. and S. S. Hsiau (2004). Dynamic behaviors of powders in a vibrated bed. *Powder Technol. 139*, 221–232.

Tang, C. and P. Bak (1988). Critical exponents and scaling relations for self-organized critical phenomena. *Phys. Rev. Lett. 60*, 2347–2350.

Tang, Y., A. J. Armstrong, R. C. Mockler, and W. J. O'Sullivan (1989). Free-expansion melting of a colloidal monolayer. *Phys. Rev. Lett. 62*, 2401–2404.

Tata, B. V. R., P. V. Rajamani, J. Chakrabarti, A. Nikolov, and D. T. Wasan (2000). Gas-liquid transition in a two-dimensional system of millimeter-sized like-charged metal balls. *Phys. Rev. Lett. 84*, 3626–3629.

Tatarski, V. I. (1961). *Wave Propagation in a Turbulent Medium*. New York: McGraw-Hill.

Thomas, B., M. O. Mason, and A. M. Squires (2000). Some behaviors of shallow vibrated beds across a wide range in particle size and their implications for powder classification. *Powder Technol. 111*, 34–49.

Thomas, B. and A. M. Squires (1998). Support for faraday's view of circulation in a fine-powder chladni heap. *Phys. Rev. Lett. 81*, 574–577.

Umbanhowar, P., F. Melo, and H. L. Swinney (1996). Localized excitations in a vertically vibrated granular layer. *Nature 382*, 793–796.

Umbanhowar, P. and H. L. Swinney (2000). Wavelength scaling and square/stripe and grain mobilty transitions in vertically oscillated granular layers. *Physica A 288*, 344–362.

van der Weele, K., M. van der Meer, M. Versluis, and D. Lohse (2001). Hysteretic clustering in granular gas. *Europhys. Lett. 53*, 328–334.

van Doorn, E. and R. P. Behringer (1997). Wavy instability in shaken sand. In R. P. Behringer and J. T. Jenkins (Eds.), *Powders & Grains 97*, Rotterdam, pp. 397–400. Balkema.

van Zon, J. S., J. Kreft, D. I. Goldman, D. Miracle, J. B. Swift, and H. L. Swinney (2004). Crucial role of sidewalls in velocity distributions in quasi-two-dimensional granular gases. *Phys. Rev. E 70*, 040301(R).

Warr, S. and J.-P. Hansen (1996). Relaxation of local density fluctuations in a fluidized granular medium. *Europhys. Lett. 36*, 589–594.

Warr, S., J. M. Huntley, and G. T. H. Jacques (1995). Fluidization of a two-dimensional granular system: Experimental study and scaling behavior. *Phys. Rev. E 52*, 5583–5595.

Wassgren, C. R., C. E. Brennen, and M. L. Hunt (1996). Vertical vibration of a deep bed of granular material in a container. *J. Appl. Mech. 63*, 712–719.

Wassgren, C. R., M. L. Hunt, and C. E. Brennen (1997). Investigation of f/2 and f/4 waves in granular beds subject to vertical, sinusoidal oscillations. In R. P. Behringer and J. T. Jenkins (Eds.), *Powders & Grains 97*, Rotterdam, pp. 433–436. Balkema.

Watanabe, H., S. Yukawa, Y. Ozeki, and N. Ito (2004). Critical exponents of isotropic-hexatic phase transition in the hard-disk system. *Phys. Rev. E 69*, 045103(R).

Whitham, G. B. (1974). *Linear and nonlinear waves*. Wiley.

Wildman, R. D. and J. M. Huntley (2000). Novel method for measurement of granular temperature distributions in two-dimensional vibro-fluidised beds. *Powder Technol. 113*, 14–22.

Wildman, R. D., J. M. Huntley, and J.-P. Hansen (1999). Self-diffusion of grains in a two-dimensional vibrofluidized bed. *Phys. Rev. E 60*, 7066–7075.

Wildman, R. D., J. M. Huntley, J.-P. Hansen, D. J. Parker, and D. A. Allen (2000). Single-particle motion in three-dimensional vibrofluidized granular beds. *Phys. Rev. E 62*, 3826–3835.

Wildman, R. D. and D. J. Parker (2002). Coexistence of two granular temperatures in binary vibrofluidized beds. *Phys. Rev. Lett. 88*(6), 064301.

Yang, X., C. Huan, D. Candela, R. W. Mair, and R. L. Walsworth (2002). Measurements of grain motion in a dense, three-dimensional granular fluid. *Phys. Rev. Lett. 88*, 044301.

Zahn, K., R. Lenke, and G. Maret (1999). Two-stage melting of paramagnetic colloidal crystals in two dimensions. *Phys. Rev. Lett. 82*, 2721–2724.

Acknowledgment

I am indepted to all those who assisted and supported me. Especially I would like to thank

- Ingo Rehberg for accepting me at his chair, his generous financial support that allowed me to purchase all the equipment I desired, and the critical comments on my work during our weekly meetings.
- Christof A. Krülle for accepting me in his group, introducing me to programming in C++, and the private and professional conversations during tea breaks and trips to our project partners.
- Jennifer Kreft, Daniel Svensek and Chi-Hwang Tai for the close and fruitful collaborations during their stays in Bayreuth.
- Rafał Grochowski and Peter Walzel for constructing the annular vibratory conveyor and Michael Grevenstette, Hamid El hor, and Stefan Linz for illuminating discussions during our project meetings .
- the members of the sand group Almudena García Sánchez, Christopher Groh, Christian Kröner, Alexander Langenbucher, Kerstin Morber, and Tobias Schnautz for extending my knowledge about the behavior of granular materials.
- my colleagues at the chair Achim Beetz, Hans Braun, Anna Butsch, Eugenio Casini, Georg Eska, Birgit Fischer, Christian Gollwitzer, Holger Knieling, Robert Krauss, Alberto de Lozar, Stefan Messlinger, Matthias Müller, Reinhard Richter, Peter Rupp, Achim Sack, Wolfgang Schöpf for their contribution to the congenial atmosphere at the workplace.
- Christine Linser for her competent help in administrative affairs, Carmen Lottes for her assistance with all kinds of experimental problems, Klaus Ötter for constructing various containers, camera mountings, and an adjustable support for the conical mirror, and Hans-Jörg Wehner for designing among other electronic devices the electro-optical camera triggering system.